

**DESIGN AND FABRICATION OF A
SINGLE LINE IQ MODULATOR**

by

Christopher J. Cullen

A thesis submitted to the Faculty of the University of Delaware in partial fulfillment of the requirements for the degree of Master of Science in Electrical and Computer Engineering.

Fall 2018

Copyright 2018 Christopher J. Cullen
All Rights Reserved

**DESIGN AND FABRICATION OF A
SINGLE LINE IQ MODULATOR**

by
Christopher J. Cullen

Approved:

Dennis W. Prather, Ph.D.
Professor in charge of thesis on behalf of the Advisory Committee

Approved:

Kenneth E. Barner, Ph.D.
Chair of the Department of Electrical and Computer Engineering

Approved:

Levi T. Thompson, Ph.D.
Dean of the College of Engineering

Approved:

Douglas J. Doren, Ph.D.
Interim Vice Provost for Graduate and Professional Education

ACKNOWLEDGMENTS

This work would not have been able to have been completed without the contribution of many people. First, I would like to thank my advisor, Dr. Dennis W. Prather for welcoming me into his group. I entered this group knowing nothing about RF photonics, barely knowing of its existence from next to no exposure from my undergraduate studies. Regardless, he provided all of the tools and encouragement necessary to lead me down a path towards success and improve my ability as a researcher. His enthusiasm for the subject and motivation to always take the extra step has provided me with a great experience from my time here, and I look forward to continue working under his guidance in the years to come.

I would also be remiss to not specifically thank Dr. Timothy Creazzo, Dr. Janusz Murakowski, and Dr. Mathew Zablocki. From before I was even officially working for the group, Mat willingly shared his expertise and knowledge to help me develop in terms of research and device fabrication. When working with Tim, his ability to find the right question to ask, and patience in explaining procedures or phenomenon that I did not understand was a serious help in progressing my research and developing my ability and drive to push and understand my work further. Janusz's extreme patience in explaining concepts and answering question I probably should have asked weeks prior has provided valuable insight both in terms of the path forward of this work and my development as a photonics researcher. The mentorship that these three have given and continue to lend is something that I seriously appreciate and cherish.

This entire experience is also something that I owe to all of my peers within the research group. The comradery that I have enjoyed and the friendships that I have formed are something that I do not take for granted. They have also lended their insight and motivation in times where I have been stuck or in continual loop of failure, and it is something that I appreciate and will continue to do so.

I finally need to thank my family and friends for their continued support and encouragement through this process. Most importantly, my parents, Jill and Jerry, and my sister, Michelle, who have always supported my decisions and work, and have been a lean-to for when times have been frustrating and difficult. Without my parents instilling the drive to show up and not settle for less than my best, I would not be where I am today.

TABLE OF CONTENTS

LIST OF TABLES	vii
LIST OF FIGURES	viii
ABSTRACT	xii

Chapter

1	INTRODUCTION	1
1.1	The Push for More Bandwidth and Ubiquitous Access	1
1.2	A Suitable Alternative to Conventional Electronic Distribution.....	2
1.3	A Proposed Solution to High Frequency Modulators	4
1.4	Thesis Outline.....	6
2	VECTOR MODULATION CONCEPT AND THEORY	7
2.1	Introduction to Vector Modulation.....	7
2.2	Theoretical Derivation of Operation	10
2.3	Propagation Model	17
2.4	Conclusion.....	24
3	BULK LITHIUM NIOABTE VECTOR MODULATOR PLATFORM.....	25
3.1	Titanium Diffused Waveguides in Bulk Lithium Niobate	25
3.2.1	Titanium Diffusion Model.....	26
3.2.2	Degenerate Mode Modeling.....	28
3.3	Ti-diffused Waveguide Device Fabrication	30
3.3.1	Ti Diffusion Optimization	33
3.4	Ti:LiNbO ₃ Waveguide Analysis.....	35
3.5	Conclusion.....	39
4	THIN-FILM LITHIUM NIOBATE VECTOR MODULATOR PLATFORM.....	40

4.1	Thin Film Lithium Niobate	40
4.2	Thin Film Waveguide Platforms	41
4.2.1	Silicon Strip-loaded Waveguide Platform.....	41
4.2.2	Silicon Nitride Strip-loaded Waveguide Platform	43
4.3	Silicon Nitride Rib Waveguide Fabrication	45
4.3.3	Silicon Nitride Deposition Development	47
4.3.2	Facet Polishing Development.....	50
4.4	Waveguide Characterization	56
4.5	Conclusion.....	59
5	DC AND RF MODULATION TESTING	60
5.1	DC Testing.....	60
5.1.1	DC Results from Ti:LiNbO ₃ platform.....	64
5.1.2	DC Results from Thin-Film LiNbO ₃ Platform.....	67
5.2	RF Characterization.....	71
5.2.1	RF and Optical Signal Paths.....	74
5.2.2	Experimental RF Results.....	76
5.3	Conclusion.....	80
6	CONCLUSION	81
6.1	Summary.....	81
6.2	Future Work.....	81
	REFERENCES	84

LIST OF TABLES

Table 3.1	Effective indices resulting from Lumerical Mode simulations	28
Table 4.1	Results of preliminary index variation inquiry.....	49
Table 4.2	List of materials and methods used for surface protection.....	54

LIST OF FIGURES

Figure 1.1	Basic photonic link consisting of laser, modulator, optical amplifier, photodiode, and antenna.	2
Figure 1.2	Proposed system using dual wavelength approach for phased array antenna feeding.	5
Figure 2.1	A vector modulator using off-the-shelf phase and amplitude modulators.	7
Figure 2.2	Electro-optic tensor of LiNbO ₃ , in pm/V.	8
Figure 2.3	Off-the-shelf vector modulator configuration for dual mode operation.	9
Figure 2.4	SLIQ modulator configuration.	10
Figure 2.5	Index ellipsoid including a section perpendicular to the direction of propagation used in a construction to find eigenmodes.	12
Figure 2.6	Application of various electric fields to a waveguide in LiNbO ₃ that has a degenerate, unperturbed initial state.	19
Figure 2.7	Visualization of right and left traveling waves into and out of a cavity.	20
Figure 2.8	Visualization of effect of modulator cavity using new model.	24
Figure 3.1	Change in refractive index related to a diffusion of 100 nm of source Ti that was 10 μm wide at 1050 °C for 10 hours.	27
Figure 3.2	TE mode profile in Ti:LiNbO ₃ waveguide.	28
Figure 3.2	Overlay of TE and TM effective indices.	30
Figure 3.3	End facet of a diced LiNbO ₃ sample A) before and B) after diamond lapping polishing.	33

Figure 3.4	Diffused Ti waveguides with 100 nm source viewed under A) light field and B) dark field illumination (*Note: Image B has color correction to make features more visible).....	34
Figure 3.5	Diffused Ti waveguides with 140 nm source viewed under A) light field and B) dark field illumination (*Note: Image B has no color correction).....	35
Figure 3.6	TE and TM FSR for a 8 μm wide, 100 nm Ti source waveguide.....	36
Figure 3.7	TE and TM mode beating in 8 μm wide, 100 nm Ti source waveguide.....	37
Figure 3.8	TE and TM FSR of 8 μm wide, 140 nm Ti source waveguide.....	38
Figure 3.9	TE and TM mixed FSR of 8 μm wide, 140 nm Ti source waveguide.....	38
Figure 4.1	Depiction of the CIS process. (A) He^+ ions are implanted into a bulk LiNbO_3 wafer; (B) the damaged wafer is bonded to another rigid handle; (C) the wafer stack is annealed and the wafer splits at the damaged region.	41
Figure 4.2	Simulated layer stack for a silicon strip-loaded waveguide on thin film LiNbO_3	42
Figure 4.3	TM mode in silicon strip-loaded waveguide.....	43
Figure 4.4	Simulated layer stack for a silicon nitride strip-loaded waveguide on thin film LiNbO_3	44
Figure 4.5	TM mode in silicon nitride strip-loaded waveguide.	45
Figure 4.6	(A) Side and (B) front illumination of failed thin film LiNbO_3 sample.....	48
Figure 4.7	Chipping on surface after initial polishing.....	50
Figure 4.8	45° polishing jig using an SEM stub.	52
Figure 4.9	Resultant end facet after 45° polish.....	52
Figure 4.10	15° polishing jig.....	53

Figure 4.11	Resultant end facet polishing at 15°	53
Figure 4.12	Facet view of protective layers after polishing.	55
Figure 4.13	Dark field illuminated image post-polishing using hard baked, 25 μm resist.	55
Figure 4.14	FSR response from TE and TM launched light in a silicon nitride ridge waveguide on thin film LiNbO ₃	56
Figure 4.15	Mixed TE/TM launched light into a silicon nitride ride waveguide on thin film LiNbO ₃	57
Figure 4.16	Fourier transform of FSR data of the TE (A) and TM (B) modes of the waveguide, with marked points of degeneracy.	58
Figure 4.17	Theoretical improvement in ellipse deformation in A) bulk LiNbO ₃ and B) thin film LiNbO ₃	59
Figure 5.1	Depiction of E-fields in GSSG electrode.	60
Figure 5.2	GSSG electrodes on a bulk Ti:LiNbO ₃ sample.	61
Figure 5.3	DC measurement test set-up showing input fibers and output fibers, needle probes, and sample under test.	63
Figure 5.4	Visualization of changing index ellipse from electric fields in the (A) vertical and (B) horizontal direction with respect to the sample surface.	64
Figure 5.5	Results of in phase signals with TM polarized light launch in bulk Ti:LiNbO ₃ platform.	65
Figure 5.6	Results of out of phase signals with TE polarized light launch in bulk Ti:LiNbO ₃ platform.	65
Figure 5.7	Unfiltered response of TE launched light with in-phase electrical stimuli on a thin film LiNbO ₃ device.	67
Figure 5.8	Filtered results of in-phase signal with TE launched light on a thin film LiNbO ₃ device.	68

Figure 5.9	Filtered results of out-of-phase signal with TM launched light on a thin film LiNbO ₃ device.	68
Figure 5.10	Mixed TE/TM optical launch with 90° offset signals on a thin film LiNbO ₃ device.	70
Figure 5.11	RF feed path to drive tested devices.....	72
Figure 5.12	Equivalent circuit representation of the RF operation on the device.	72
Figure 5.13	High frequency electrodes on a thin film LiNbO ₃ device.....	74
Figure 5.14	Optical components and signal flow used for device measurement.....	75
Figure 5.15	Collected data from TE launched light into a thin film LiNbO ₃ device with 4 GHz excitation.	77
Figure 5.16	Collected data from TM launched light into a thin film LiNbO ₃ device with 4 GHz excitation.	77
Figure 5.17	Normalized response of thin film LiNbO ₃ at 4 GHz excitation.	78
Figure 6.1	Proposed facet etching fabrication flow. (A) Coat sample in chrome and cover with resist; (B) etch back chrome to expose damaged device layer and etch using an ICP-RIE resulting in (C); (D) remove chrome and resist masks.	82
Figure 6.2	Split GSSG electrode concept.	83

ABSTRACT

As the demand for high speed and uninterrupted access to data increases, the push for higher bandwidth, higher frequency distribution systems with increased coverage is becoming more necessary. The next generation of systems require improved size, weight, and power (SWaP) characteristics as well as wide band performance that make it difficult for current all-electronic solutions to remain the primary method of distribution, particularly with the desire to push into the millimeter wave (mmW) regime. This is where the microwave photonic approach through the means of optical links begins to show major benefits.

In this work, the development of a unique single line in-phase and quadrature-phase (SLIQ) vector modulator is proposed to meet the requirements of a possible photonic link architecture that conforms to the current trends in wireless communication. This device utilizes a single waveguide to achieve the required phase and amplitude modulation needed to transmit signal vectors. This SLIQ design is chosen to overcome the challenges of size and parasitic power consumption inherent to the use of currently available, off the shelf components. The operation of the SLIQ device is derived using the material platform of lithium niobate (LiNbO_3), a material used for electro-optic modulation. The device platforms of titanium-diffused waveguides in bulk LiNbO_3 and strip-loaded waveguides on thin-film LiNbO_3 have their viability and effectiveness explored and both platforms are fabricated in parallel. Fabricated devices are tested and both are shown to exhibit the desirable properties required for a SLIQ modulation. It is found though that silicon nitride strip loaded

waveguides on the thin film LiNbO_3 platform provide the most desirable operation properties for a SLIQ modulator.

Chapter 1

INTRODUCTION

1.1 The Push for More Bandwidth and Ubiquitous Access

The demand for bandwidth is pushing wireless communication networks toward ever higher frequencies and to incorporate RF beam forming to increase network capacity in the era of 5G technologies. Meanwhile, fiber optics have been ousting conventional copper in relatable applications due to their inherent low loss, high bandwidth, and limited dispersion [1], [2]. As time pushes forward, antennas, and specifically phased arrays, are expected to have a decrease in overall size, weight, and cost (SWaP) and increase in bandwidth to follow suit with the push towards millimeter wave (mmW) communication standards, as the FCC recently allocated new bands spanning 24-91 GHz specifically for 5G applications [3], [4].

At mmW frequencies, loss starts becoming a prevalent issue for all electronic signals. As frequencies rise higher and higher, atmospheric losses become a major consideration [5]. Also, as the wavelength shrinks, objects such as foliage and rain drops begin to scatter signals, increasing the overall channel loss [6]. With this increase in signal degradation, the infrastructure will require change from a cellular density of 10 base stations per square kilometer for 4G, up to 50 base stations per square kilometer to maintain the proper coverage [7]. With this increase in the number of base stations in mind, any savings in weight and cost will be highly coveted.

1.2 A Suitable Alternative to Conventional Electronic Distribution

With its inherent decrease in size and weight, and the ubiquitous use of fiber, microwave photonics can be an interesting and viable solution to address the trends and requirements of future distribution systems. In Figure 1.1, a basic RF photonic link is shown consisting of a laser, an external amplitude modulator, an erbium doped fiber amplifier (EDFA), a photodiode, and an antenna.

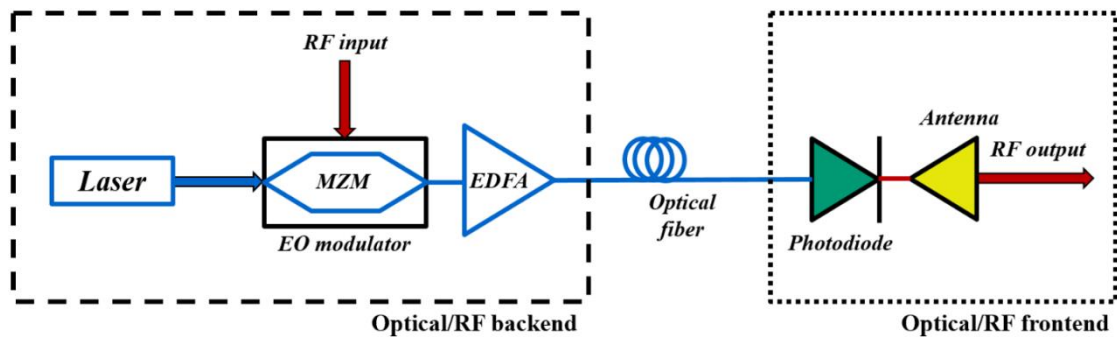


Figure 1.1 Basic photonic link consisting of laser, modulator, optical amplifier, photodiode, and antenna.

The modulator in the back-end is responsible for imparting information and upconverting the RF data signal to the optical domain, and the photodiode at the frontend optically downconverts the signal back to RF frequencies for wireless transmission. Compared to the use of coaxial cable, fiber offers very little loss regardless of the RF frequency needed for communication. This also allows for centralized localization of the optical/RF backend and easy remoting of the optical/RF front end, a benefit that could be leveraged in dense urban areas where space is at a premium.

With the trends in distribution also moving towards phased arrays antennas from isotropic radiators, photonic systems begin to shine and become worth their weight in copper, literally. Each element in an array requires its own feed, both in optical and conventional electronic systems. As the number of elements in an array rises, so does the number of feed lines to the frontend. With fiber weighing roughly 0.1 lb/m and coaxial cable anywhere from 0.13 lb/m to 3 lb/m, the weight in electronic fed arrays begins to seriously affect structural design, leading to added cost in higher strength and more rigid materials to bear the total weight of the system [8], [9].

On top of the increase in signal feeds, each antenna in an electronic array would require a high frequency mixer behind each element. At mmW frequencies, coaxial cable becomes too lossy to send the radiating frequency at any length for sufficient power at the antenna. As a result, an intermediate frequency (IF) signal with the data is sent to the antenna. Just behind the antenna is a mixer with an oscillator set to the radiating frequency, and the IF data signal is upconverted before being radiated. Not only does the need for mixers and oscillators increase the size, weight, and cost per element of the array, the system requires precise control of the amplitude and phase of the oscillators. For a phased array to work, radiating signals all need to exhibit the same phase such that they constructively interfere on the output. Complex monitoring and control of each local oscillator would be required so that all of the signals remain phase coherent, a problem that scales in cost and complexity with both number of elements and increasing frequencies. The issue of coherence is inherently addressed in an RF- photonic-based system. By simply using one laser and splitting it N times (N being the number of channels) to drive the entire system, the need for complex phase control is removed, as the system maintains the phase set by the laser.

To make the simple photonic link shown in Figure 1.1 viable for phased array applications, phase modulators are required on a per channel basis. This allows for control of the phase of light in a channel, which controls how the signal interferes at the output and forms the desired RF beam. By coupling a phase and an amplitude modulator to use creative encoding schemes, multiple special multiplexed data signals can be transmitted at once using a phased array system. However, creating high efficiency, high frequency modulators is not a simple task, and because of this, an alternate optical backend is proposed.

1.3 A Proposed Solution to High Frequency Modulators

To remove the need for high speed modulators, a system using a dual optical wavelength approach is proposed, as shown in Figure 1.2.

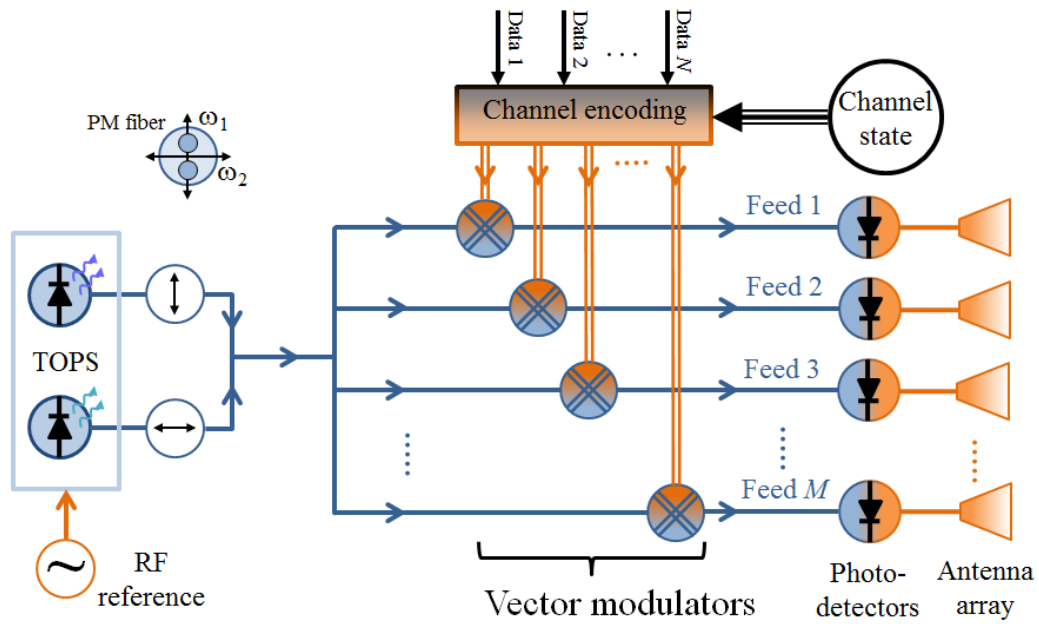


Figure 1.2 Proposed system using dual wavelength approach for phased array antenna feeding.

Utilizing the tunable optical paired source (TOPS) system designed by Dr. Prather's group at the University of Delaware, an RF carrier can be generated optically where a pair of lasers emit light offset in wavelength. The lasers are correlated (phase locked) using injection locking, and the difference in wavelength (frequency) is determined by a local RF reference source [10]. This wavelength separation in the carrier allows the vector modulator to only be responsible for functioning at modulation speeds of that of the encoding scheme, which is limited by that of the digital-to-analog (DAC) in the channel encoder.

1.4 Thesis Outline

The focus of this research is to develop, fabricate, and test a novel vector modulator design that could be used in the proposed phased array system in the previous section. The starting point of this work is with the operating theory and simulating of the proposed modulator design in Chapter 2. Chapters 3 and 4 offer bulk lithium niobate (LiNbO_3) and thin-film LiNbO_3 as platforms for realizing the proposed modulator design. The platforms will have their fabrication methodologies explained and their feasibility to perform as vector modulators predicted. Chapter 5 covers the testing of the fabricated devices from the previous chapters at DC and RF excitation, and their results are analyzed. Finally, in Chapter 6, the main points of the thesis are summarized, and some avenues of continued device improvement are elaborated upon.

Chapter 2

VECTOR MODULATION CONCEPT AND THEORY

2.1 Introduction to Vector Modulation

Vector modulation is the task of taking a signal vector, which consists of both phase and amplitude data (also referred to as the in-phase and quadrature phase, or IQ) and imparting it onto an optical beam. This modulation can be done using off-the-shelf components of phase modulators and amplitude modulators, shown in Figure 2.1.

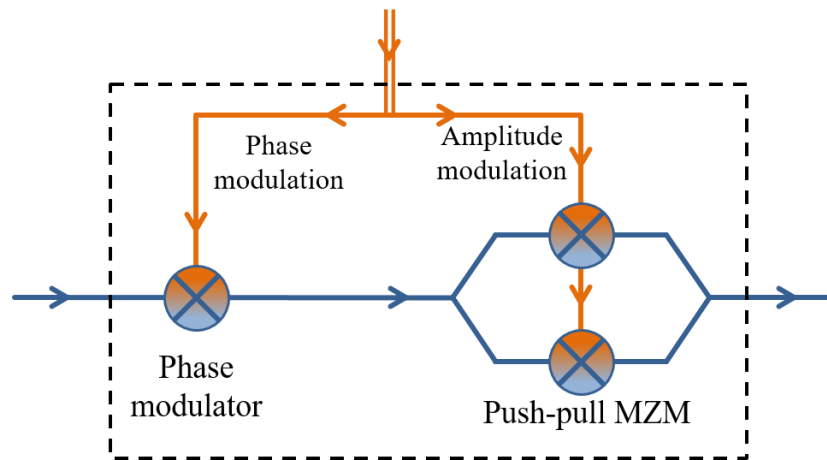


Figure 2.1 A vector modulator using off-the-shelf phase and amplitude modulators.

A common material used for modulators is lithium niobate (LiNbO_3), due to its relatively high electro-optic coefficients (EO), shown from the EO tensor of the material in Figure 2.2.

$$\begin{pmatrix} r_{ij} \end{pmatrix} = \begin{pmatrix} \cdot & \circ & \bullet \\ \cdot & \bullet & \bullet \\ \cdot & \cdot & \cdot \\ \cdot & \bullet & \cdot \\ \bullet & \cdot & \cdot \\ \circ & \cdot & \cdot \end{pmatrix} \quad \begin{array}{l} r_{13} = 8.6 \\ r_{22} = 3.4 \\ r_{33} = 30 \\ r_{51} = 28 \end{array}$$

Figure 2.2 Electro-optic tensor of LiNbO₃, in pm/V.

In single mode operation, modulators in LiNbO₃ are generally oriented so that the highest value of 30 pm/V, exhibited by r_{33} , is used. This is referred to as z-cut. However, in the system proposed previously, two orthogonal optical modes are used. When this is the case, one mode is subject to r_{33} , and the other to the smaller r_{13} . When subject to excitation, the different values of the electro-optic tensor manifest themselves as a relative phase difference between the two modes. More detail on why this phenomenon happens is explained in following section. This relative phase difference can be utilized by the off-the-shelf vector modulator architecture to still achieve vector modulation with the addition of a polarizer to the design, shown in Figure 2.3.

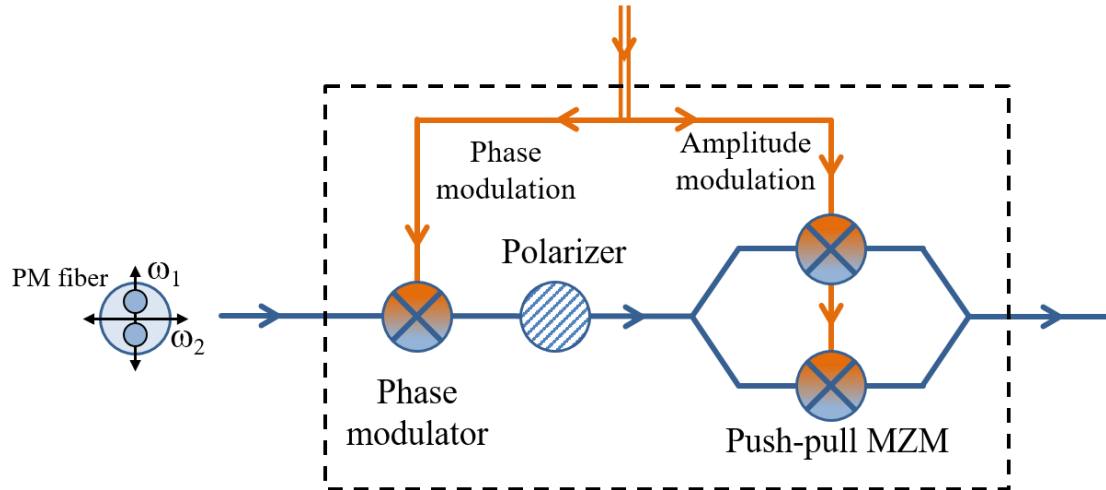


Figure 2.3 Off-the-shelf vector modulator configuration for dual mode operation.

The polarizer's purpose is to project the two modes onto a single axis such that the push-pull Mach-Zehnder modulator (MZM) will impart amplitude modulation without further affecting the relative phase of the two modes. While effective, two major drawbacks of this architecture are size and power consumption. The size of off-the-shelf modulators range from 2.5 inches to 3.75 inches, resulting in a total vector modulator size of at least 5 inches [11]–[13]. Also, for MZMs to work in their linear regime, they need to be biased in quadrature. To maintain quadrature biasing, some kind of monitoring and feedback circuitry is required, creating a parasitic power draw on the system that scales with array size.

To address these issues, a single device that does both phase *and* amplitude modulation is proposed in the form of a single line IQ modulator (SLIQ-M) that utilizes dual optical mode operation in a single waveguide through the entire device.

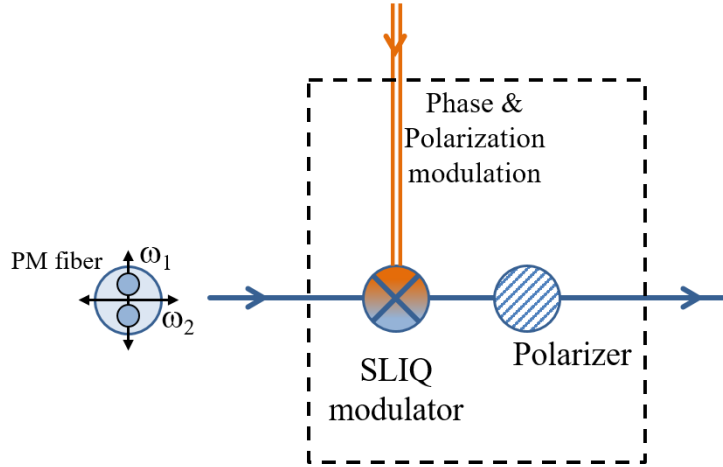


Figure 2.4 SLIQ modulator configuration.

The configuration proposed in Figure 2.4 shows a device that receives two orthogonal optical modes and a combined data signal that includes both phase and polarization modulation information. The polarization modulation is mapped into amplitude modulation with the use of the polarizer. The development of the SLIQ-M envelops the rest of this thesis, with the next sections describing in depth the theory and operation of a SLIQ device.

2.2 Theoretical Derivation of Operation

Lithium niobate (LiNbO_3) is a uniaxial birefringent material with the ordinary index $n_o = 2.214$ and the extraordinary index $n_e = 2.138$ [14], with the z crystalline direction identified as the optical axis. Accordingly, the index ellipsoid of lithium niobate is oblate with the axis of rotation coinciding with the optic axis. The introduction of a waveguide into the LiNbO_3 material changes the default birefringence. In particular, the effective refractive index of a mode propagating in a waveguide patterned in the vicinity of a surface is reduced due to the interaction with

the low index of the cladding, for example, air. In this case, the index of the TE mode is generally reduced by a greater amount than that of the TM mode. For x -cut LiNbO_3 wafers, where the waveguide direction is perpendicular to the x -axis, the variance in the refractive index change effectively induces biaxial birefringence in the material. As a result, the effective index ellipsoid has a general shape with three distinct axes. Such an index ellipsoid may be described using the following equation:

$$\left(\frac{1}{n^2}\right)_1 x^2 + \left(\frac{1}{n^2}\right)_2 y^2 + \left(\frac{1}{n^2}\right)_3 z^2 + 2\left(\frac{1}{n^2}\right)_4 yz + 2\left(\frac{1}{n^2}\right)_5 xz + 2\left(\frac{1}{n^2}\right)_6 xy = 1, \quad (2.1)$$

where the axes x, y, z are oriented so that in the absence of an external electric field, the last three terms on the left-hand side are zero. The relation simplifies with proper orientation to:

$$\left(\frac{1}{n^2}\right)_1 x^2 + \left(\frac{1}{n^2}\right)_2 y^2 + \left(\frac{1}{n^2}\right)_3 z^2 = 1. \quad (2.2)$$

Equations (2.1) and (2.2) may be cast in the matrix form of:

$$(x, y, z) \mathbf{B} \begin{pmatrix} x \\ y \\ z \end{pmatrix} = 1, \quad (2.3)$$

with a properly defined matrix B . For continued analysis, it is assumed B takes on the form

$$B = \begin{pmatrix} \left(\frac{1}{n^2}\right)_1 & 0 & 0 \\ 0 & \left(\frac{1}{n^2}\right)_2 & 0 \\ 0 & 0 & \left(\frac{1}{n^2}\right)_3 \end{pmatrix}, \quad (2.4)$$

so that Eq. (2.2) can be recovered.

The eigenmodes and the corresponding effective refractive indices for a given direction of propagation are found by taking a section of this index ellipsoid with a plane perpendicular to the direction of propagation. Then, identifying the main axes of the resulting ellipse as the polarizations of the eigenmodes, the lengths of these axes are equal to the respective indices of refraction. Figure 2.5 shows an example of an index ellipsoid along with a k -vector and the corresponding ellipsoidal section.

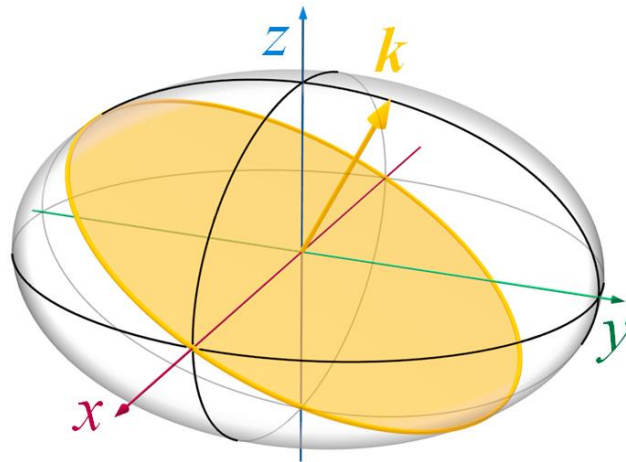


Figure 2.5 Index ellipsoid including a section perpendicular to the direction of propagation used in a construction to find eigenmodes.

For x -cut LiNbO₃, where interest lies in propagation along a direction in the yz plane, the eigenmodes may be obtained by rotating the system of coordinates in the yz plane, and finding the cross-section by setting $z = 0$. The rotation of the system of coordinates is achieved by sandwiching matrix B between the rotation matrix:

$$R_\phi = \begin{pmatrix} 1 & 0 & 0 \\ 0 & \cos \phi & -\sin \phi \\ 0 & \sin \phi & \cos \phi \end{pmatrix}, \quad (2.5)$$

and its transpose, $R_\phi^T B R_\phi$, to obtain the following equation for the index-ellipsoid in the rotated coordinates

$$(x, y, z) R_\phi^T B R_\phi \begin{pmatrix} x \\ y \\ z \end{pmatrix} = 1. \quad (2.6)$$

This may be explicitly written as:

$$\begin{aligned} & \left(\frac{1}{n^2}\right)_1 x^2 + \left[\left(\frac{1}{n^2}\right)_2 \cos^2 \phi + \left(\frac{1}{n^2}\right)_3 \sin^2 \phi \right] y^2 + \left[\left(\frac{1}{n^2}\right)_2 \sin^2 \phi + \left(\frac{1}{n^2}\right)_3 \cos^2 \phi \right] z^2 + \\ & + \left[\left(\frac{1}{n^2}\right)_3 - \left(\frac{1}{n^2}\right)_2 \right] \sin(2\phi) yz = 1. \end{aligned} \quad (2.7)$$

The equation for the ellipse, obtained from Eq. (2.7) by sectioning this index ellipsoid with a plane perpendicular to the z -axis, is found by setting $z = 0$:

$$\left(\frac{1}{n^2}\right)_1 x^2 + \left[\left(\frac{1}{n^2}\right)_2 \cos^2 \phi + \left(\frac{1}{n^2}\right)_3 \sin^2 \phi \right] y^2 = 1. \quad (2.8)$$

From Eq. (2.8), it is found that the effective index for the TM mode is $n_I' = n_I$, the same as for the propagation along the original z direction, whereas the effective index for the TE mode depends on angle ϕ as follows:

$$\left(\frac{1}{n^2}\right)_1 x^2 + \left[\left(\frac{1}{n^2}\right)_2 \cos^2 \phi + \left(\frac{1}{n^2}\right)_3 \sin^2 \phi\right] y^2 = 1. \quad (2.9)$$

In the SLIQ vector modulator, angle ϕ is chosen to ensure degeneracy, realized as $n_I' = n_2'$.

Electric field $\mathbf{E} = (E_1, E_2, E_3)^T$ deforms the index ellipsoid by modifying the coefficients in Eq. (2.1) as follows:

$$\begin{pmatrix} \Delta\left(\frac{1}{n^2}\right)_1 \\ \Delta\left(\frac{1}{n^2}\right)_2 \\ \Delta\left(\frac{1}{n^2}\right)_3 \\ \Delta\left(\frac{1}{n^2}\right)_4 \\ \Delta\left(\frac{1}{n^2}\right)_5 \\ \Delta\left(\frac{1}{n^2}\right)_6 \end{pmatrix} = \begin{pmatrix} r_{11} & r_{12} & r_{13} \\ r_{21} & r_{22} & r_{23} \\ r_{31} & r_{32} & r_{33} \\ r_{41} & r_{42} & r_{43} \\ r_{51} & r_{52} & r_{53} \\ r_{61} & r_{62} & r_{63} \end{pmatrix} \begin{pmatrix} E_1 \\ E_2 \\ E_3 \end{pmatrix}, \quad (2.10)$$

where r_{ij} are the electro-optic coefficients of LiNbO₃. Using matrix notation, the equation defining the deformed index ellipsoid in the presence of external electric field may be written as:

$$(x, y, z)(B + \Delta) \begin{pmatrix} x \\ y \\ z \end{pmatrix} = 1, \quad (2.11)$$

where

$$\Delta = \sum_{j=1}^3 E_j \mathbf{r}_j, \text{ and } \mathbf{r}_j = \begin{pmatrix} r_{1j} & r_{6j} & r_{5j} \\ r_{6j} & r_{2j} & r_{4j} \\ r_{5j} & r_{4j} & r_{3j} \end{pmatrix}. \quad (2.12)$$

The eigenmodes corresponding to the ellipsoid deformed by the applied electric field are obtained in the same way as above: rotate the coordinates by angle φ and section the ellipsoid with a plane defined by $z = 0$. Following Eq. (2.6), the equation for rotated system of coordinates is:

$$(x, y, z) R_\phi^T (B + \Delta) R_\phi \begin{pmatrix} x \\ y \\ z \end{pmatrix} = 1, \quad (2.13)$$

whereas the specific form of the equation for the ellipse depends on the direction of the applied electric field. The field directions relevant to the present case include the direction perpendicular to the surface, which in the case of an x -cut wafer is E_x and the in-plane direction perpendicular to the direction of propagation, which contains both E_y and E_z components of the electric field, and will be referred to as E_s . Substituting Eq. (2.12) into (2.13) with E_x as the only non-vanishing component of the electric

field, and setting $z = 0$, to obtain the section yields the following equation for the corresponding ellipse:

$$\left(\frac{1}{n^2}\right)_1 x^2 + \left[\left(\frac{1}{n^2}\right)_2 \cos^2 \phi + \left(\frac{1}{n^2}\right)_3 \sin^2 \phi\right] y^2 + 2E_x (r_{61} \cos \phi + r_{51} \sin \phi) xy = 1. \quad (2.14)$$

For the electric field parallel to the surface and perpendicular to the direction of propagation, the same procedure yields the following equation for the corresponding ellipse:

$$\left[\left(\frac{1}{n^2}\right)_1 + (r_{13} \sin \phi - r_{22} \cos \phi) E_s\right] x^2 + \left[\left(\frac{1}{n^2}\right)_2 \cos^2 \phi + \left(\frac{1}{n^2}\right)_3 \sin^2 \phi + (r_{22} \cos^3 \phi + (r_{13} + 2r_{51}) \cos^2 \phi \sin \phi + r_{33} \sin^3 \phi) E_s\right] y^2 = 1. \quad (2.15)$$

Equations (2.14) and (2.15) are the basis for the decisions going forward as to which specific designs of the vector modulator are viable.

First, it is noted that according to Eq. (2.14), the application of the electric field along the x direction introduces a cross term into the equation for the ellipse given in Eq. (2.8). Assuming that care is taken to select the angle ϕ so that the ellipse is actually a circle:

$$\left(\frac{1}{n^2}\right)_1 = \left(\frac{1}{n^2}\right)_2 \cos^2 \phi + \left(\frac{1}{n^2}\right)_3 \sin^2 \phi, \quad (2.16)$$

where the cross term $2E_x (r_{61} \cos \phi + r_{51} \sin \phi)xy$ causes squeezing and stretching of the circle along diagonal directions. As a result, the polarization of the eigenmodes is tilted by $\pm 45^\circ$ with respect to the x -axis, in the direction perpendicular to the surface of the x -cut wafer. Therefore, a TE mode launched into such a waveguide will “leak” into the TM mode, and vice versa, under the application of electric field. In other words, the TE and TM modes become coupled and the strength of this coupling is proportional to the electric field component E_x . Note that the mode coupling is also proportional to $(r_{61} \cos \phi + r_{51} \sin \phi)$, where angle ϕ is measured from the crystalline z -axis.

In the vector modulator, the conversion from TE to TM, and vice versa, has the effect of polarization rotation, which, in combination with a linear polarizer at the modulator output, can be used to obtain direct modulation of intensity. The efficiency of the amplitude modulation is proportional to $(r_{61} \cos \phi + r_{51} \sin \phi)$.

The modulation of the relative phase between the TE and TM modes is obtained by the application of the electric field in plane, labeled as E_s in Eq. (2.15). According to Eq. (2.15), the TE and TM modes remain the eigenmodes of the waveguide under the application of E_s field. However, the effective refractive index of the TM and TE modes changes according to terms $(r_{13} \sin \phi - r_{22} \cos \phi)E_s$ and $(r_{22} \cos^3 \phi + (r_{13} + 2r_{51}) \cos^2 \phi \sin \phi + r_{33} \sin^3 \phi)E_s$, respectively. Therefore, generally, modulation of the relative phase between TE and TM mode takes place under the application of electric field E_s .

2.3. Propagation Model

To understand how light would propagate through a vector modulator using a single waveguide, a representation of the deforming index ellipse phenomenon

was needed. Deformation of the index ellipse is described by the following equation, which accounts for the initial state of the index ellipse (in this case, degeneracy), and an electric field applied in an arbitrary direction:

$$\begin{aligned} & \left[\left(\frac{1}{n^2} \right)_1 + \underbrace{(r_{13} \sin \theta - r_{22} \cos \theta) E_s}_{\mathbf{A}} \right] x'^2 + \\ & \left[\left(\frac{1}{n^2} \right)_2 \cos^2 \theta + \left(\frac{1}{n^2} \right)_2 \sin^2 \theta + \underbrace{(r_{22} \cos^3 \theta + (r_{13} + 2r_{51}) \cos^2 \theta \sin \theta + r_{33} \sin^3 \theta) E_s}_{\mathbf{C}} \right] y'^2 + \\ & 2E_p \underbrace{(r_{61} \cos \theta + r_{51} \sin \theta)}_{\mathbf{B}} x' y' = 1, \end{aligned} \quad (2.17)$$

where E_s and E_p are the applied electric fields in the horizontal and vertical direction, respectively, θ is the angle of the waveguide from the crystalline z direction, r_{ij} are the various EO coefficients of LiNbO₃, x' and y' are the orthogonal axis in the plane of optical signal propagation, and n_1 , n_2 , and n_3 , are the effective indices for light polarized in the crystalline x , y , and z direction, respectively. The **A** and **C** sections of the equation correspond to the change in the ellipse in the x' and y' direction respectively, and the **B** coefficient corresponds to change 45° between the x' and y' axes. Knowing this, the ellipse can be described as the following matrix relation:

$$\begin{bmatrix} x' & y' \end{bmatrix} \begin{bmatrix} A & B \\ B & C \end{bmatrix} \begin{bmatrix} x' \\ y' \end{bmatrix} = 1. \quad (2.18)$$

Finding the eigenvalues and eigenvectors of the $\begin{bmatrix} A & B \\ B & C \end{bmatrix}$ matrix results in

the new values of the principle axis of the ellipse and the rotation of the new axis from

the orthogonal x' and y' axis, respectively. In short, this information gives the major and minor axis the index ellipse and the values to use in a rotation matrix to apply the effective indices to a Cartesian axis. Figure 2.6 shows how applying various electric fields to a degenerate mode waveguide in LiNbO_3 changes the index ellipse.

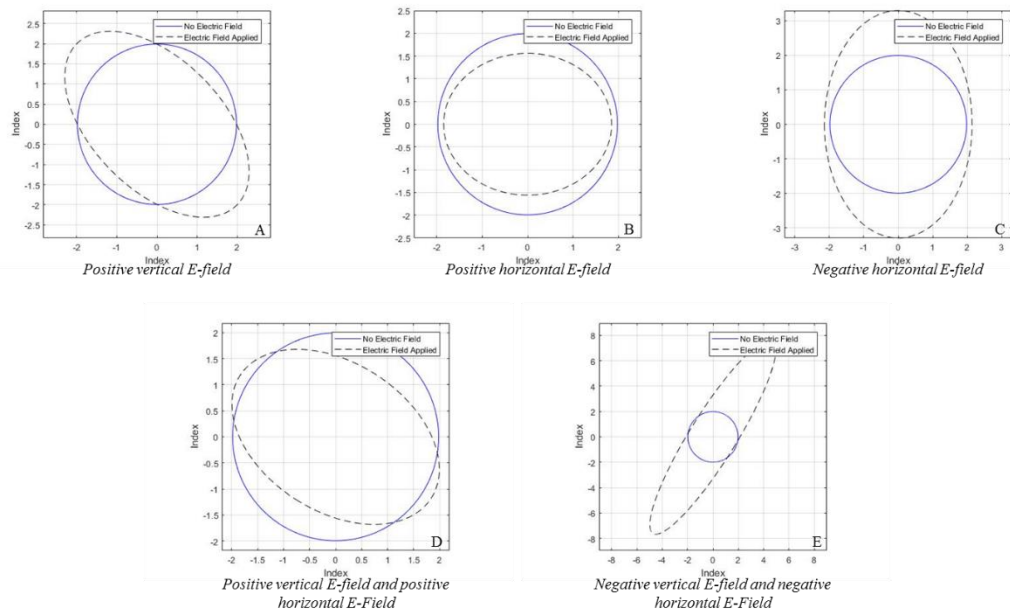


Figure 2.6 Application of various electric fields to a waveguide in LiNbO_3 that has a degenerate, unperturbed initial state.

Development of the model begins with describing the system as a collection of right and left traveling waves as visualized in Figure 2.7.

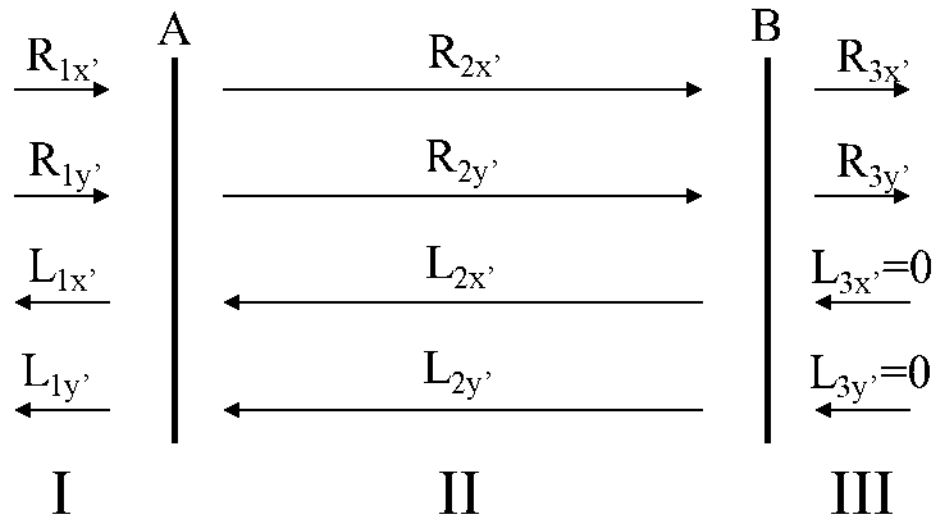


Figure 2.7 Visualization of right and left traveling waves into and out of a cavity.

In this system, the light in the direction of both x' and y' needs to be considered since intended operation requires polarization rotation. In the model, the following assumptions were made: right and left traveling waves do not interfere with each other, the horizontal and vertical components of the index do not interact with each other at the interface, and the scattering caused by interface **A** and **B** have inverse responses. The last two assumptions currently only allow this model to work for devices with perfectly perpendicular facets.

Using the information from the index ellipse covered in Section 2.2., the system can be described as:

$$\begin{bmatrix} R_{3x'} \\ R_{3y'} \\ L_{3x'} \\ L_{3y'} \end{bmatrix} = \underbrace{R_\phi^{-1} X_b P X_a R_\phi}_{P_{\text{sys}}} \begin{bmatrix} R_{1x'} \\ R_{1y'} \\ L_{1x'} \\ L_{1y'} \end{bmatrix}, \quad (2.19)$$

where

$$R_\phi = \begin{bmatrix} \cos(\phi) & -\sin(\phi) & 0 & 0 \\ \sin(\phi) & \cos(\phi) & 0 & 0 \\ 0 & 0 & \cos(\phi) & -\sin(\phi) \\ 0 & 0 & \sin(\phi) & \cos(\phi) \end{bmatrix}, \quad (2.20)$$

$$P = \begin{bmatrix} P_{11}^{+x} & 0 & 0 & 0 \\ 0 & P_{22}^{+y} & 0 & 0 \\ 0 & 0 & P_{33}^{-x} & 0 \\ 0 & 0 & 0 & P_{44}^{-y} \end{bmatrix}, \quad (2.21)$$

$$X_a = \begin{bmatrix} X_{11} & 0 & X_{13} & 0 \\ 0 & X_{22} & 0 & X_{24} \\ X_{31} & 0 & X_{33} & 0 \\ 0 & X_{42} & 0 & X_{44} \end{bmatrix}, \quad (2.22)$$

and

$$X_b = X_a^{-1}. \quad (2.23)$$

R_ϕ is the rotation matrix, determined from finding the eigenvectors of the **ABBC** matrix that describes the perturbed index ellipse in Eq. (2.18), where ϕ is the angle of rotation from the propagation axes of the input light. R_ϕ^{-1} is the inverse of R_ϕ , used to

return the system back to the normal Cartesian axes, P is the propagation matrix through region II (see Figure 2.7), and each non-zero element is in the form of $e^{-\left(j\frac{2\pi}{\lambda}n'_i l\right)}$, where λ is the free-space wavelength, n'_i is the perturbed index oriented in the minor or major axis, and l is the length of the active region of the device. X_a represents the scattering parameters at the “A” interface (see Figure 2.7). Each term is calculated by determining the reflection and transmission coefficient for a given electric field at the interface. The relation given in Equation (2.23) requires the given assumptions made previously, that since the facets are flat, the reflection and transmission parameters are inverses of the each other. All of these terms together constitute what will referred to as P_{sys} .

The next assumption made to simplify the system is that there is no light being reflected back into the system in region III. This is used to remove the dependence of requiring the knowledge of the values of the left traveling waves in the system. To realize this assumption, the inverse relation of the system must be calculated:

$$\begin{bmatrix} R_{1x'} \\ R_{1y'} \\ L_{1x'} \\ L_{1y'} \end{bmatrix} = P_{sys}^{-1} \begin{bmatrix} R_{3x'} \\ R_{3y'} \\ L_{3x'} = 0 \\ L_{3y'} = 0 \end{bmatrix} \rightarrow \begin{bmatrix} R_{1x'} \\ R_{1y'} \\ L_{1x'} \\ L_{1y'} \end{bmatrix} = \begin{bmatrix} iP_{sys11} & iP_{sys12} & iP_{sys13} & iP_{sys14} \\ iP_{sys21} & iP_{sys22} & iP_{sys23} & iP_{sys24} \\ iP_{sys31} & iP_{sys32} & iP_{sys33} & iP_{sys34} \\ iP_{sys41} & iP_{sys42} & iP_{sys43} & iP_{sys44} \end{bmatrix} \begin{bmatrix} R_{3x'} \\ R_{3y'} \\ 0 \\ 0 \end{bmatrix} \quad (2.24)$$

where iP_{sysij} is the ij^{th} value of the P_{sys}^{-1} matrix. In this particular case, only the terms that contribute to right traveling waves are desired, leaving the following as the only relevant terms:

$$\begin{bmatrix} R_{1x'} \\ R_{1y'} \\ L_{1x'} \\ L_{1y'} \end{bmatrix} = \begin{bmatrix} iP_{\text{sys}11} & iP_{\text{sys}12} & iP_{\text{sys}13} & iP_{\text{sys}14} \\ iP_{\text{sys}21} & iP_{\text{sys}22} & iP_{\text{sys}23} & iP_{\text{sys}24} \end{bmatrix} \begin{bmatrix} R_{3x'} \\ R_{3y'} \\ 0 \\ 0 \end{bmatrix}. \quad (2.25)$$

This relation can be simplified even further still since the dependence on the knowledge of the left traveling waves is being removed, leaving only

$$\begin{bmatrix} R_{1x'} \\ R_{1y'} \end{bmatrix} = \begin{bmatrix} iP_{\text{sys}11} & iP_{\text{sys}12} \\ iP_{\text{sys}21} & iP_{\text{sys}22} \end{bmatrix} \begin{bmatrix} R_{3x'} \\ R_{3y'} \end{bmatrix}. \quad (2.26)$$

To complete the model, dependency on the input light in region I must be restored, which results in the final relation being

$$\begin{bmatrix} R_{3x'} \\ R_{3y'} \end{bmatrix} = \begin{bmatrix} iP_{\text{sys}11} & iP_{\text{sys}12} \\ iP_{\text{sys}21} & iP_{\text{sys}22} \end{bmatrix}^{-1} \begin{bmatrix} R_{1x'} \\ R_{1y'} \end{bmatrix}. \quad (2.27)$$

In Figure 2.8, the effects of the mathematical model can be seen using various states of input polarization and directions of applied electric field.

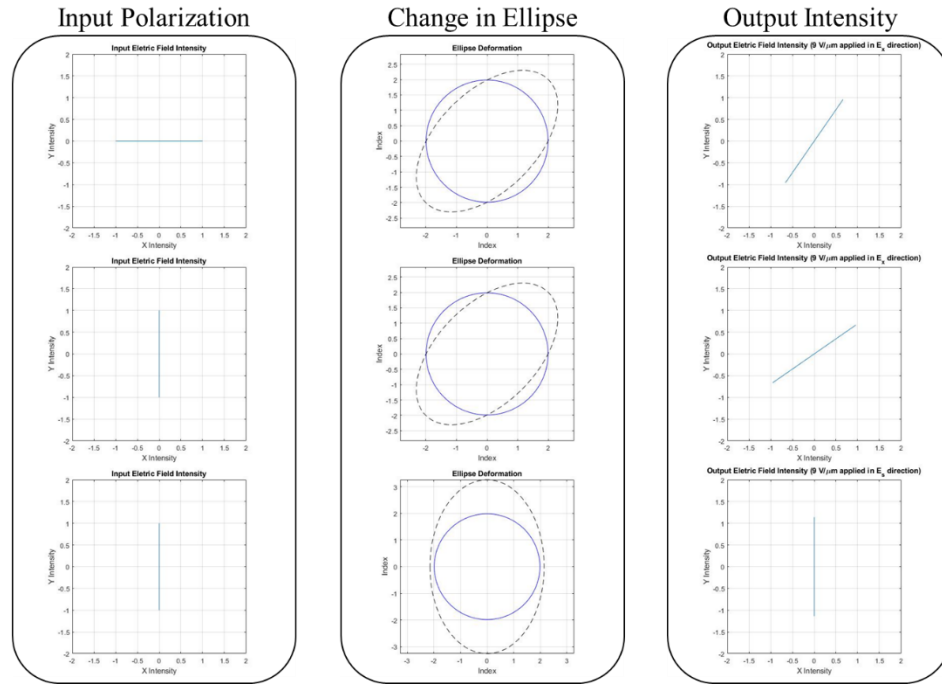


Figure 2.8 Visualization of effect of modulator cavity using new model.

In the above figure, the response of the output is as expected. When the change in the index ellipse is 45° between the eigenmodes, polarization rotation should occur, and when the change in the ellipse is in the direction of the eigenmodes, only phase modulation and no polarization rotation should occur.

2.4 Conclusion

It can be seen that a SLIQ vector modulator architecture is a viable method for performing the needed phase and amplitude modulation needed for vector modulation. The sections that immediately follow delve into the various material platforms investigated to create this single waveguide device.

Chapter 3

BULK LITHIUM NIOABTE VECTOR MODULATOR PLATFORM

Lithium niobate (LiNbO_3) is a unique material that offers piezoelectric, ferroelectric, and EO qualities. It offers a broad window of transmission offering low transmission losses between $0.2 \mu\text{m}$ to $12 \mu\text{m}$ [15]. To guide waves through the material, titanium in-diffusion [16], [17] and annealed proton exchange [18], [19] offer the means of creating a small index change needed to allow confinement. Its non-centrosymmetric crystal structure allow it to exhibit Pockel's effect, which makes it very useful as a modulating material, which is elaborated upon in detail in the previous chapter.

Having now understood the operating principles of the vector modulator, creation of a physical device was desired. The first device made was in bulk LiNbO_3 due to its ready availability and extensive knowledge of fabrication in Dr. Prather's group. Presented in this chapter is the development of a diffusion model of titanium in LiNbO_3 for optical waveguiding, the degenerate mode modeling of the $\text{Ti}:\text{LiNbO}_3$ platform, the description of device fabrication, and waveguide characterization.

3.1 Titanium Diffused Waveguides in Bulk Lithium Niobate

Waveguiding in LiNbO_3 is often achieved by the means of in-diffusing titanium (Ti), as it introduces low loss, typically around $\sim 0.1 \text{ dB/cm}$ [20]. The presence of Ti on the surface of LiNbO_3 in a heated, oxygen rich environment promote the out-diffusion of lithium and allow the in-diffusion of Ti, creating a graded index region required for guiding light [21]. The following sections describe the development of a diffusion model to accurately calculate the effective index of

Ti:LiNbO₃, and the optical simulation performed to find the required angle for optical mode degeneracy.

3.2.1 Titanium Diffusion Model

The model explained represents the situation where a rectangular Ti strip of finite thickness is deposited on top of a LiNbO₃ substrate as a source, and is completely consumed at the completion of the diffusion. The concentration of the Ti diffused into LiNbO₃ from the surface follows Eq (3.28):

$$C = \frac{1}{2} C_0 \exp\left(-\frac{y^2}{D_s^2}\right) \left[\operatorname{erf}\left(\frac{\frac{w}{2} - x}{D_b}\right) + \operatorname{erf}\left(\frac{\frac{w}{2} + x}{D_b}\right) \right], \quad (3.28)$$

where C_0 is the initial Ti ion concentration, D_s and D_b are the diffusion lengths along the surface and into the bulk, respectively, w is the initial width of the Ti strip, and x and y are the distances into the bulk and along the surface of the LiNbO₃, respectively. The value of the initial Ti ion concentration C_0 is obtained from [22]:

$$C_0 = \frac{t}{1.559 \times 10^{23} \cdot D_b}, \quad (3.29)$$

where t is the initial thickness of the Ti strip. The diffusion lengths for the model are obtained from [22]:

$$D_x = \sqrt{TD_{0x} \exp\left(\frac{-E_{ax}}{kT_{Diff}}\right)}, \quad (3.30)$$

where D_x represents the diffusion length either into the bulk or along the surface, T represent the total diffusion time, D_{0x} represents the diffusion coefficient of Ti into LiNbO₃ either into the bulk or along the surface, E_{ax} represented the activation energy of Ti into LiNbO₃ either into the bulk or along the surface, k is Boltzmann's constant, and T_{Diff} is the diffusion temperature. For the simulation of the waveguide oriented along the y direction, D_{0b} was $1.1e-1$ and D_{0s} was $1.7e-5$ [22]. For the simulation where the waveguide was oriented along the z direction, D_{0b} was $1.2e-1$ and D_{0s} was $4.1e-4$ [22]. Using Eq (3.28) through (3.30), and the constituent constants associated with the Ti:LiNbO₃ diffusion process, two-dimensional concentration profiles were obtained using MATLAB. These concentrations were then mapped to changes in index, resulting in Gaussian-elliptical curves as seen in Figure 3.1.

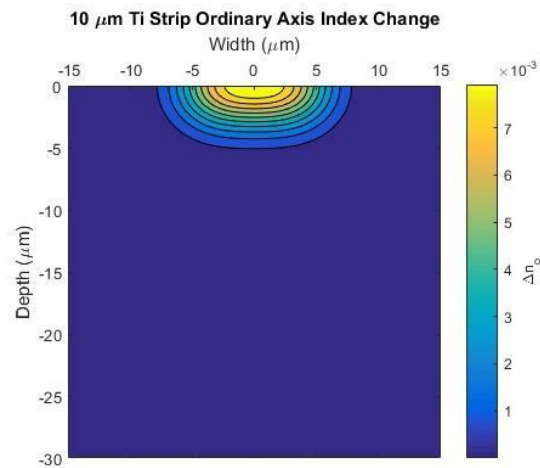


Figure 3.1 Change in refractive index related to a diffusion of 100 nm of source Ti that was 10 μm wide at 1050 $^{\circ}\text{C}$ for 10 hours.

3.2.2 Degenerate Mode Modeling

After modeling the refractive index change for waveguides oriented along both the y and z axis of an x -cut lithium niobate wafer, the results were imported into the Lumerical Mode solver. The effective indices simulated were obtained from a model comprising a 100 nm thick Ti source that was 8 μm wide, diffused at 1050 $^{\circ}\text{C}$ for 10 hours, fabrication parameters that were used previously with z -cut lithium niobate wafers in the group. The effective refractive indices for TE and TM modes and propagation along x and y directions are shown in Table 3.1, and the mode profile is shown in Figure 3.2.

Table 3.1 Effective indices resulting from Lumerical Mode simulations

	y Propagation	z Propagation
TE Effective Index	2.144835	2.214590
TM Effective Index	2.214563	2.214411

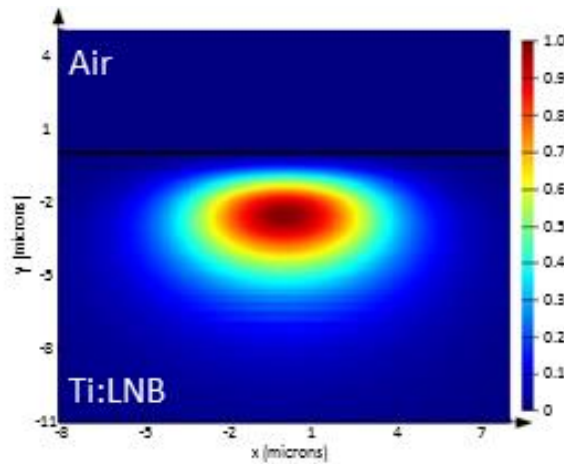


Figure 3.2 TE mode profile in Ti:LiNbO_3 waveguide.

Note that the indices for both TM and TE modes corresponding to z propagation direction are all nearly identical. These propagation directions and polarizations align the propagating light to the ordinary refractive index in bulk LiNbO_3 . The differences in the simulated device stem from the interaction of the mode with the surface and from the concentration gradient of the diffused Ti. The index for the TE mode resulting from propagation in y direction corresponds to the extraordinary index in bulk LiNbO_3 ; it is lower than the other effective indices, as expected from their bulk values.

Further, note that the TE index for y propagation is lower than the corresponding TM index, whereas the opposite is true for z propagation. As a result of this crossover between the modes, there will be some angled waveguide orientation that allows for the TE and TM modal indices to be the same. To interpolate between the simulated values of refractive index, the relation given in Eq (2.16) was used. The interpolations were then overlaid and their intersection points were observed. The functions and intersect points, which are at roughly two degrees off the z -axis of the crystal, can be seen in Figure 3.2. This means that a waveguide patterned two degrees off of the z -axis will result in a degenerate waveguide.

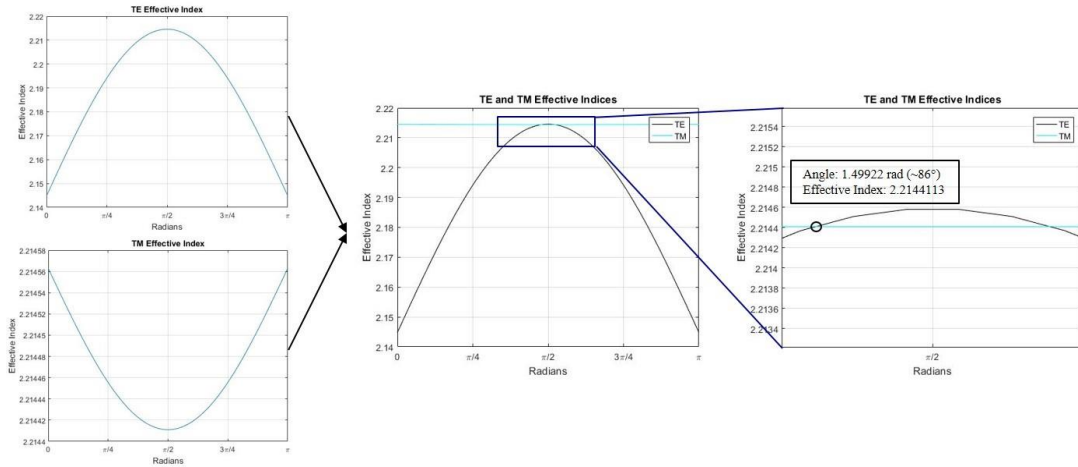


Figure 3.2 Overlay of TE and TM effective indices.

This small angle from the z -axis of the crystal means that waveguide masks designed to travel straight along the z -axis have a high probability of being aligned $\sim 2^\circ$ off the crystal axis. This is due to the error in the machining of the wafer flats from Gooch and Housgo, the provider of the LiNbO_3 wafers [23], and the inherent human error present during manual alignment.

3.3 Ti-diffused Waveguide Device Fabrication

The first step in fabrication is the cleaning of an x -cut LiNbO_3 wafer. This is done using a piranha solution ($\text{H}_2\text{SO}_4:\text{H}_2\text{O}_2$, 3:1) to eliminate any organics that are on the surface. Second, the wafer is prepped for UV contact lithography. This is done by casting the negative lift-off photoresist NR9-1000PY from Futurrex at 3000 RPM for 45 seconds, achieving a resist thickness of approximately $1 \mu\text{m}$. After casting, the wafer is slowed to 2000 RPM, and edge bead removal is done by ejecting acetone from a syringe onto the outer edge of the device. This is to remove the bead of photoresist that collects and swells at the edge of the sample which prevents uniform

mask contact during contact lithography. The resist then has to be soft baked to evaporate the solvents so that the film can harden. This is done on a hot plate set to 150 °C for 2 minutes. The wafer is then aligned under a photomask in a mask aligner to ensure the waveguides were aligned to the appropriate wafer flat of LiNbO₃ wafer. Once aligned, the wafer is brought into contact with the photomask and the wafer is exposed with a dose of 85 mJ/cm² at a 365 nm wavelength. A post exposure bake is then required to crosslink the exposed resist, and this is done on a hot plate set at 100 °C for 2 minutes. It is then developed using RD6 from Futurrex, which contains tetramethylammonium hydroxide (TMAH) for 30 seconds.

After lithography, the next step is to deposit Ti onto the surface. Before deposition though, the wafer must go through a descum process to remove any residual resist in the “valley” of the transferred pattern. This is accomplished by using a dry-cleaning process in a barrel asher. The wafer is inserted into the reaction chamber, and the chamber is pumped down to a backpressure of 3 Pa and 12 sccm of oxygen (O₂) is introduced. The gas is excited using 150 W of RF power, and the sample remains in this environment for 4 minutes. Next, the wafer is placed in the evaporator. Here, a nominal thickness of 100 nm of Ti is deposited on the sample using electron beam evaporation.

Following Ti deposition, the wafer goes through a lift-off process. This involves soaking the wafer in a 300 mL beaker of acetone until the Ti visually begins to separate from the sample surface. At this point, a wash bottle of acetone is used to agitate the surface of the acetone in the beaker to prevent the Ti from re-bonding to the surface of the LiNbO₃ due to van der Waal interactions [24]. Mitigation of this re-deposition is crucial because if any portion of the Ti strip bonds to a critical area of the

wafer e.g. the waveguiding region, it will diffuse into the LiNbO_3 and alter the optical mode during testing, effectively rendering the waveguide, and possibly a whole area, useless. There is currently no method known to remove the re-deposited Ti. After all the Ti has lifted off, the wafer is removed from the acetone bath and doused in methanol and isopropyl alcohol so that no resist residue redeposits on the surface that was suspended in the acetone. The wafer is dried using a nitrogen (N_2) blowgun to ensure complete evaporation of the isopropyl alcohol.

The wafer is then loaded into the diffusion furnace. The wafer is placed into the center of a wafer boat and is surrounded by silicon wafers on both sides to promote laminar flow around the wafer. The diffusion chamber is then flooded with N_2 as the temperature rises to 600 °C. From 600 °C to 1050 °C, the N_2 flow is terminated, and O_2 is added to the environment. The chamber then soaks at 1050 °C for 10 hours. The chamber is then ramped down to 600 °C in the O_2 environment, and for the remainder of the cooling to room temperature, the full N_2 atmosphere is reintroduced.

Before the waveguides could be characterized, the wafers needed to be diced. The surface was coated with NR9-3000PY from Futurrex, cast at 1000 RPM for 45 seconds, resulting in a resist thickness of around 4 μm . It was then hard baked at 150 °C for 5 minutes, then diced into 10 mm by 10 mm squares. Since dicing leaves chipping at the edges of the facet, polishing is required to promote the coupling of light into the waveguide. This was accomplished using diamond grit coated lapping films on a rotating platten. The effects of this polishing can be seen in Figure 3.3.

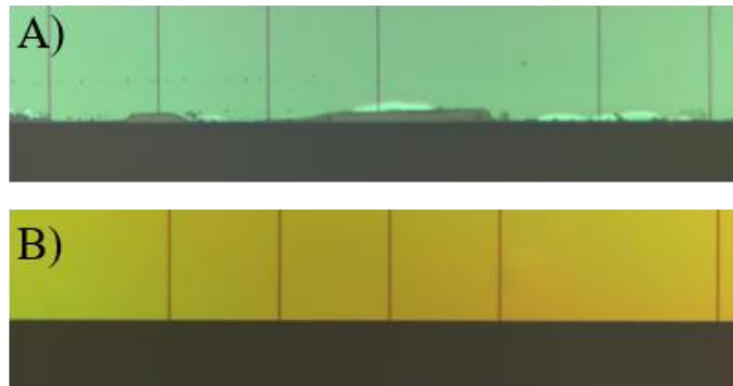


Figure 3.3 End facet of a diced LiNbO₃ sample A) before and B) after diamond lapping polishing.

3.3.1 Ti Diffusion Optimization

A battery of tests were completed on diffusing titanium into *x*-cut LiNbO₃. This was to determine the maximum amount of Ti that could be diffused into LiNbO₃ without leaving excess source on the surface. Determining the thickness of Ti to diffuse was necessary, as not enough source material results in low mode confinement which increases loss through the device. In addition, excessive source material leaves titanium oxide (an artifact of the Ti:LiNbO₃ in-diffusion mechanism) on the LiNbO₃ surface which also contributes to loss in the device. Ti thickness of 40 nm, 60 nm, 80 nm, 100 nm, 120 nm, and 140 nm were deposited onto separate wafers. The wafers were then diffused at 1050 °C for 10 hours in an oxygen rich atmosphere, in accordance to the fabrication process described in Section 3.3. Post diffusion, the wafers were inspected under a microscope to look for edge roughness and other defects.

When viewing the wafers optically, roughness around the side walls and on surface of the waveguides are inspected, which gives indication of incomplete consumption of the Ti source. Samples that have complete source consumption generally are invisible while looking under dark field and have very faint features while viewing under light field. Figure 3.4 shows the 100 nm titanium source wafer, which displayed indication of complete source consumption, under light and dark field illumination.

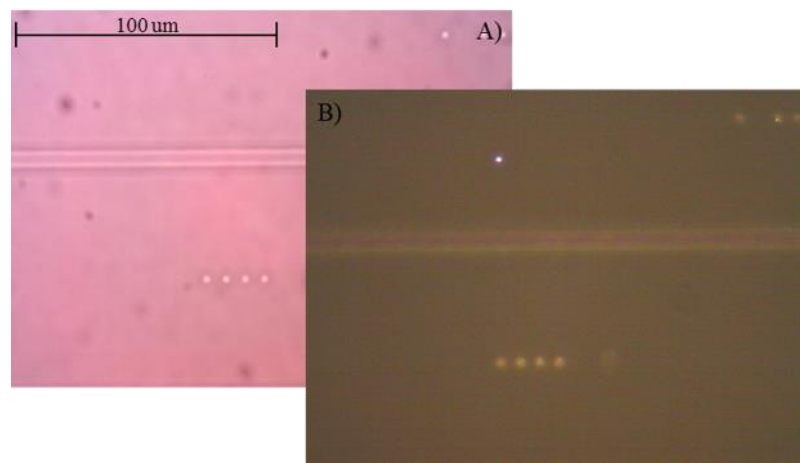


Figure 3.4 Diffused Ti waveguides with 100 nm source viewed under A) light field and B) dark field illumination (*Note: Image B has color correction to make features more visible).

All the source thicknesses showed complete diffusion, with only the 140 nm source beginning to show indication of incomplete diffusion. The indication of incomplete diffusion is shown by the slight waveguide profile illumination while viewing the sample under a dark field microscope. This profile can be seen in Figure 3.5.

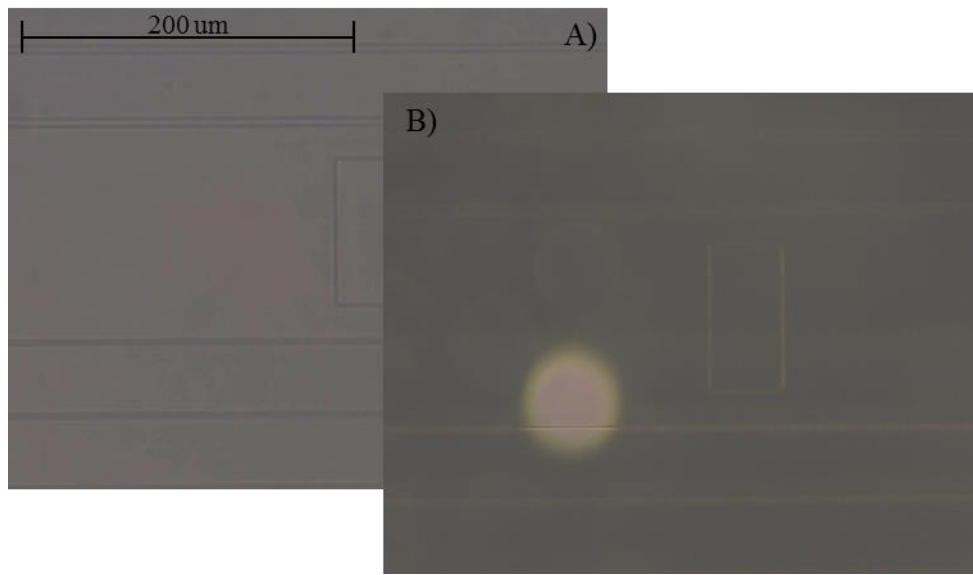


Figure 3.5 Diffused Ti waveguides with 140 nm source viewed under A) light field and B) dark field illumination (*Note: Image B has no color correction).

Proceeding this optimization, to ensure that a large amount of Ti source was not remaining on the surface of the sample, atomic force microscopy (AFM) was used to see if any appreciable height variation in the surface that could be measured, and none could be detected by the tool. This is indication of no Ti remaining on the surface.

3.4 Ti:LiNbO₃ Waveguide Analysis

To evaluate the properties of the diffused waveguides, a fiber-to-fiber measurement system was used to measure the free spectral range (FSR) of the waveguide samples. TE and TM polarized light was launched into various width waveguides and titanium thicknesses. The output from a C-band tunable laser was coupled into and out of the samples under test using a 6.5 μm spot sized lens fiber, whose slow axis was keyed to the TM mode (vertical polarization) of the waveguide, into a InGaAs photodetector. A polarization rotator in the form of a vertical polarizer

and a half-wave plate was used to orientate and rotate the incoming light such that there was minimal amount of mode mixing in the sample. The tunable laser was swept such that optical transmission as a function of wavelength could be measured. Reflections from the ends of the sample created a Fabry-Perot cavity, and oscillations in optical intensity resulted. To minimize the effect of cavities being formed in the transmission fibers, all fibers in the system had angle-polished connectors. Figure 3.6 below shows the TE and TM free spectral range (FSR) of the 8 μm wide, 100 nm Ti source waveguide.

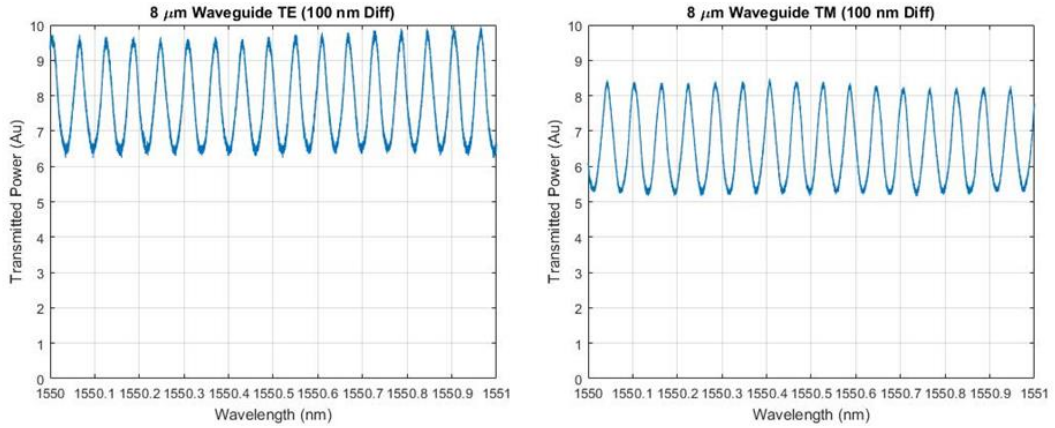


Figure 3.6 TE and TM FSR for a 8 μm wide, 100 nm Ti source waveguide.

From these oscillations, the group index could be found using the equation for Fabry-Perot resonance, which follows:

$$\Delta\nu_{FSR} = \frac{c}{n_g 2L}, \quad (3.31)$$

where $\Delta\nu_{\text{FSR}}$ is the frequency spacing between the oscillation peaks, c is the speed of light, n_g is the group velocity, and L which is the round trip path length (two times the length of the physical cavity) [25]. Solving for n_g for both the TE and TM modes, the indices were 2.092516 and 2.018663, respectively. This gives an index difference of 0.073853, about two orders of magnitude off from the simulated difference of 0.00179 (simulations completed in Lumerical MODE solver).

In conjunction with obtaining the pure TE and TM mode FSR, light was launched to obtain a FSR of the modes mixed together. With both modes excited, a beat frequency that is indicative of the difference of the TE and TM modes occurs. Figure 3.7 shows the mixed mode beating from the 8 μm wide, 100 nm Ti source waveguide.

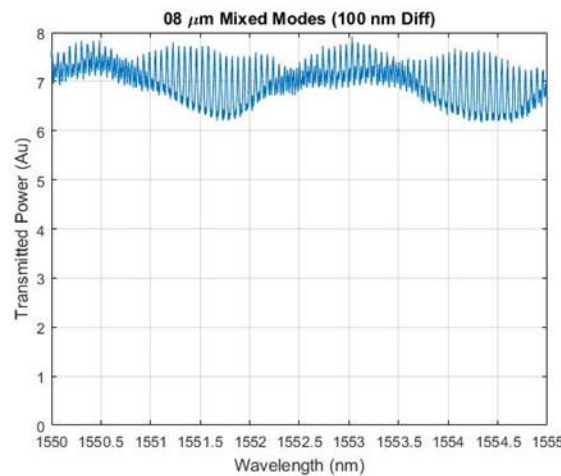


Figure 3.7 TE and TM mode beating in 8 μm wide, 100 nm Ti source waveguide.

It was observed that there is tertiary beat that appears approximately every $2.75 \mu\text{m}$. In Figure 3.8, the TE and TM mode from the $8 \mu\text{m}$ wide, 140 nm Ti source waveguide are displayed, and Figure 3.9 shows the mixing of the two modes.

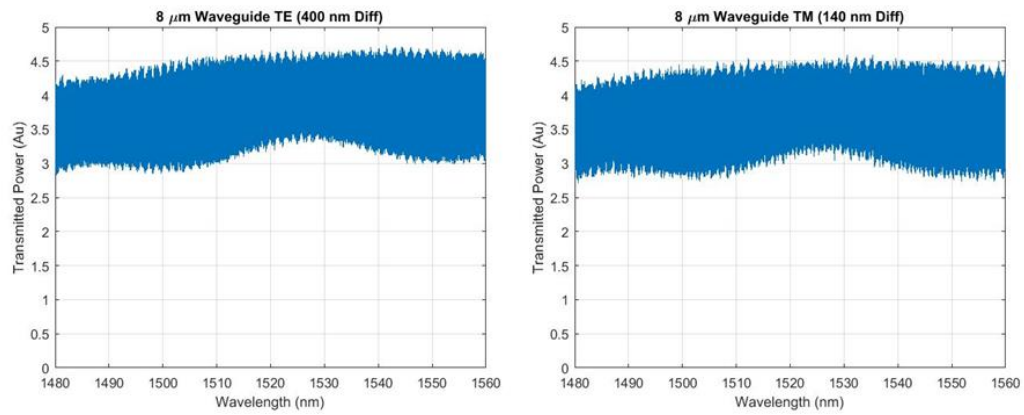


Figure 3.8 TE and TM FSR of $8 \mu\text{m}$ wide, 140 nm Ti source waveguide.

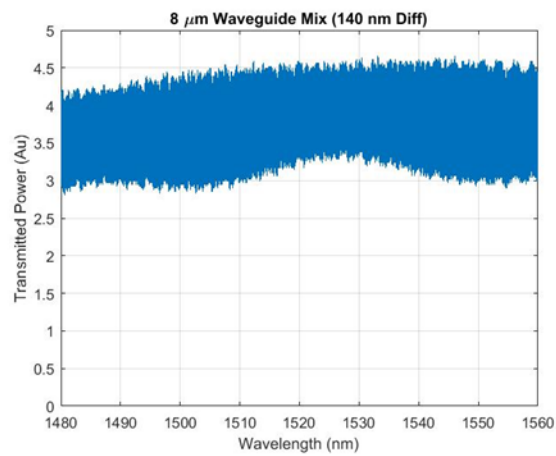


Figure 3.9 TE and TM mixed FSR of $8 \mu\text{m}$ wide, 140 nm Ti source waveguide.

From the FSR in Figure 3.8, the peaks from the cavity can be seen protruding from the core of the data. When the two modes are mixed in Figure 3.9, there is no obvious beating from the two modes. This could indicate that the modes are very close to being identical, and that the wavelength sweep wasn't long enough to capture the beating, or that the FSR is being masked by another unknown phenomenon. All things considered, this is good indication of mode degeneracy being achieved in the device. From these observations, and in observations in Section 3.3.1, a 140 nm source for diffusion was used for fabrication of this waveguiding platform.

3.5 Conclusion

The degenerate mode waveguide is shown to be a realizable structure using the conventional Ti:LiNbO₃ platform. Detailed explanations of waveguide simulation, device fabrication, and waveguide characterization were given. Although shown to accomplish the desired degeneracy, the proposed thin-film LiNbO₃ modulators expanded on in the coming chapters prove to be a more effective alternative to the bulk platform.

Chapter 4

THIN-FILM LITHIUM NIOBATE VECTOR MODULATOR PLATFORM

4.1 Thin Film Lithium Niobate

Use of thin-film LiNbO_3 as a substrate provides lateral confinement of optical modes not able to be achieved in a bulk LiNbO_3 platform. There are multiple methods of creating thin-films of LiNbO_3 , including sputtering [26], [27], Sol-gel processing [28], [29], liquid phase epitaxy [30], and vapor transport [31]. While these methods may offer the formation of high quality, stoichiometric films, crystal ion slicing (CIS) offers the ability to create larger, monocrystalline films. This method was used to obtain material used for this work.

To create an ion-slice film, helium ions (He^+) are implanted into a bulk LiNbO_3 substrate, creating a damage center in the crystal. Once implanted, the sample is then bonded to an insulator coated LiNbO_3 wafer or another material that exhibits a similar coefficient of thermal expansion, such as fused silica or quartz. This is done so that when processing is complete, the thin-film remains structurally intact and does not crack. After bonding, the sample is annealed and the crystal separates at the damaged junction. The annealing process can also serve as a method of repairing the damage done to the crystal by the ion implantation process. The CIS LiNbO_3 fabrication process is depicted Figure 4.1.

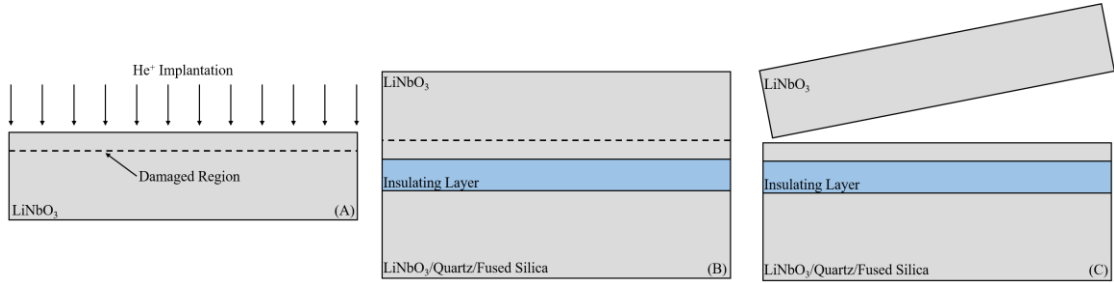


Figure 4.1 Depiction of the CIS process. (A) He^+ ions are implanted into a bulk LiNbO_3 wafer; (B) the damaged wafer is bonded to another rigid handle; (C) the wafer stack is annealed and the wafer splits at the damaged region.

The CIS LiNbO_3 used for this work was bonded to a quartz handle with a $15\ \mu\text{m}$ silicon dioxide insulating layer and was obtained from NanoLN.

4.2 Thin Film Waveguide Platforms

A typical method for confining light horizontally in a material is loading the waveguiding region of the device with another foreign material. Two methods of creating strip-loaded waveguides are further explained in this section.

4.2.1 Silicon Strip-loaded Waveguide Platform

One material often used for creating a strip-loaded waveguide is silicon. First, to achieve supporting TE and TM modes, the LNB must either have a ridge etched or be thinned to sub-micron thicknesses. Since crystal ion slicing allows thicknesses down to $600\ \text{nm}$ to be produced, it was the method pursued in simulating viable strip loaded designs. Because of silicon's high index ($n \sim 3.4$), strip dimensions had to be kept small so as to maintain a single mode in the TE and TM polarizations. Also, for the relation in Eq (2.16) to remain true, the index while propagating in TM

must remain between the indices found for the TE mode while propagating in the y and z direction. To meet all these requirements, a silicon strip of 200 nm wide and 200 nm thick was simulated above 600 nm thick LNB on a quartz handle, depicted in Figure 4.2.

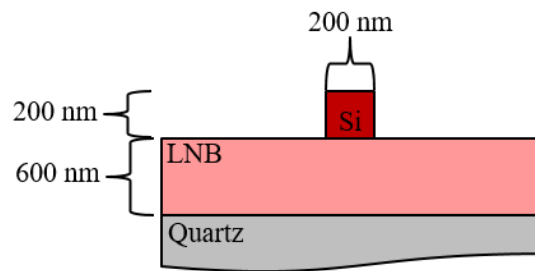


Figure 4.2 Simulated layer stack for a silicon strip-loaded waveguide on thin film LiNbO_3 .

The simulated results gave a TM index (in both y and z propagation) of 1.979003 and TM indices of 1.960218 in the y direction and 2.035270 in the z direction. Using Eq. (2.16), the rotation from the z axis is found to be $\sim 60^\circ$. This means that r_{51} is now dominant, when referring to Eq. (2.17), which is desirable. While this may seem like a viable solution, the TM mode placement is problematic, shown in Figure 4.3.

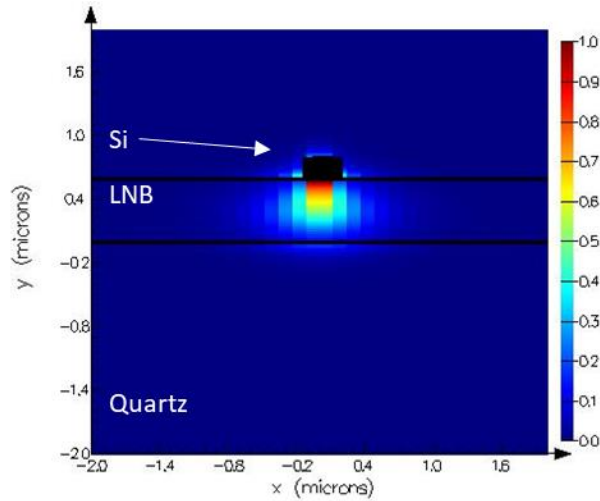


Figure 4.3 TM mode in silicon strip-loaded waveguide.

From Figure 4.3, what is seen in the LiNbO_3 is the tail of the mode, where the majority of the energy is maintained in the silicon strip. Because of this, the modulating efficiency of the TM mode would be greatly reduced, and another strip-loading architecture is required.

4.2.2 Silicon Nitride Strip-loaded Waveguide Platform

A silicon nitride strip is another viable option for strip loading the thin film lithium niobate. Silicon nitride has an index of approximately 1.9 and, because of its lower index, strip dimensions to support single TE and TM modes are larger and, thus, easier to fabricate. Silicon nitride is also amorphous and can be deposited via CVD techniques directly onto LiNbO_3 , unlike silicon, which cannot be deposited directly onto the surface due to mismatch in the LiNbO_3 and silicon lattice, and would need to be bonded. Because of the lower index, the resultant effective indices of the modes are going to be closer to the index of an optical fiber ($n \sim 1.45$), allowing more

efficient coupling out-of and into the fiber. Another benefit to using silicon nitride over silicon is reduced loss. Silicon nitride exhibits loss figures around 0.01 dB/cm, while silicon shows loss around 1.0 dB/cm [32].

The silicon nitride strip-loaded waveguide still requires a LiNbO_3 thickness of 600 nm to support the most efficient TE and TM mode, but the restriction of dimensions to maintain a TM effective index between the TE indices is lifted due to its index being lower than both the ordinary and extraordinary of LNB. Now, the only dimension constraints are those to maintain a single TE and TM mode. Silicon nitride strip dimensions that meet this requirement are 1.6 μm wide and 200 nm thick, shown in Figure 4.4.

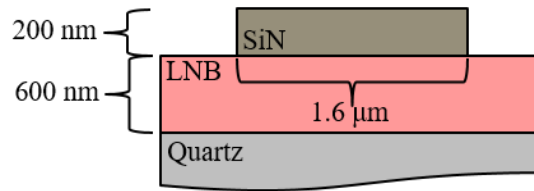


Figure 4.4 Simulated layer stack for a silicon nitride strip-loaded waveguide on thin film LiNbO_3 .

Simulated results gave a TM index (in both y and z propagation) of 1.988180 and TM indices of 1.980155 in the y direction and 2.050380 in the z direction. Using Eq. (2.16), the rotation from the z axis is $\sim 70^\circ$. Not only is r_{51} the dominant term from Eq. (2.17), the resultant value of the entire \mathbf{B} coefficient is larger than when using the silicon rib strip-loaded platform. Also, the TM (as well as the TE) are both confined mostly to the LNB, seen in Figure 4.5, which may result in a high modulation efficiency for both TE and TM modes.

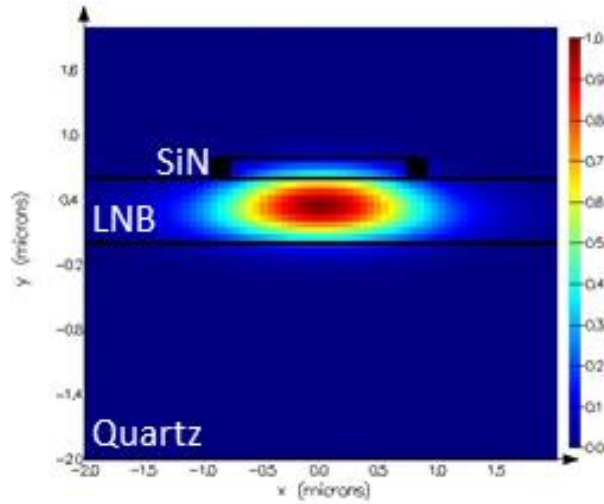


Figure 4.5 TM mode in silicon nitride strip-loaded waveguide.

Due to the advantages of using silicon nitride as a strip-load over a silicon strip-load, from this point forward, research efforts will be focused on developing the thin-film variation of the modulator with silicon nitride. However, due to limitations of on-hand materials, the device developed in the remainder of this thesis had a thin-film LiNbO_3 thickness of 700 nm. This effectively shifts the ideal waveguide angle for mode degeneracy from $\sim 70^\circ$ to $\sim 50^\circ$ for degeneracy, but provides the same fabrication steps and development needed for 600 nm use case.

4.3 Silicon Nitride Rib Waveguide Fabrication

The first step in device fabrication was cleaning an x -cut, thin film LiNbO_3 wafer with a piranha solution ($\text{H}_2\text{SO}_4:\text{H}_2\text{O}_2$, 3:1) to remove all organic material on the surface of the wafer. The sample was then cast with NR9-3000P from Futurrex at 2200 RPM for 45 seconds, resulting in a resist film of $\sim 5 \mu\text{m}$ to create a protective layer for dicing. The wafer was then diced into smaller segments along the

crystalline axis. The individual samples were then stripped of their protective resist in a piranha solution. Next, the samples underwent an oxygen plasma clean and silicon nitride deposition in a plasma enhanced chemical vapor deposition (PECVD) system. After measuring the index of the silicon nitride, the samples were cleaned using an acetone, methanol, isopropyl (AMI) rinse and PR1-2000A resist was cast at 5000 RPM for 45 seconds, resulting in a film thickness of $\sim 1 \mu\text{m}$. The samples were then soft baked on a hot plate set to $120 \text{ }^\circ\text{C}$ for 2 minutes to evaporate the solvents in the resist and harden the film. The samples were then aligned under the appropriate angled waveguide, brought into contact with the exposure mask, and exposed under 365 nm UV light at a dose of 115 mJ. Post exposure, development was done using RD6 for 40 seconds. This lithography step was to create ridges to be used as an etch mask that defines the waveguiding ribs in the silicon nitride. Next, etching of the silicon nitride occurred in an inductively couple plasma, reactive ion etcher (ICP-RIE). The etch consisted of 5 sccm sulfur hexafluoride (SF_6), 5 sccm octafluorocyclobutane (C_4F_8), and 90 sccm argon (Ar) at relative chamber pressure of 1.5 Pa. The gasses were subject to 500 of ICP RF power and an RF bias of 150 W. To etch through all 200 nm of the silicon nitride, the process lasted 1 minute and 16 seconds. The remaining resist mask was stripped off using an AMI rinse and another protective layer of resist was spun onto the surface. The samples then underwent another dicing step to create facets perpendicular to waveguides (which are not along the crystalline axis) and resulted in a device that was 10 mm by 10 mm. The resist was then removed with another AMI. Finally, the samples were spun with another protective resist layer, and were polished using physical lapping. The following sections dive deeper in to the challenges and development of the silicon nitride deposition process and recipe as

well as the techniques used to develop a useable end facet on the completed waveguiding devices.

4.3.3 Silicon Nitride Deposition Development

Initially, there were intentions of using low pressure chemical vapor deposition (LPCVD) to coat thin LiNbO_3 samples with silicon nitride since due to its ability to deposit stoichiometric, low loss silicon nitride. However, a drawback to using this form of deposition was that required temperatures during processing ranged from 700 °C to 900 °C [33], [34]. This became a concern as the maximum temperature the thin film LiNbO_3 wafers were subject to during processing at the manufacturer was approximately 350 °C. With such a large discrepancy in temperatures, thermal stress testing was done on pieces of the thin film LiNbO_3 . The samples were placed in a 2" furnace at room temperature. The furnace was set to rise to 750 °C with no defined temperature ramp and maintained that temperature for 4 hours. Post high temperature baking, the samples were found with delaminated portions of LiNbO_3 from the insulator and sections that has flaked off completely, as shown in Figure 4.6.

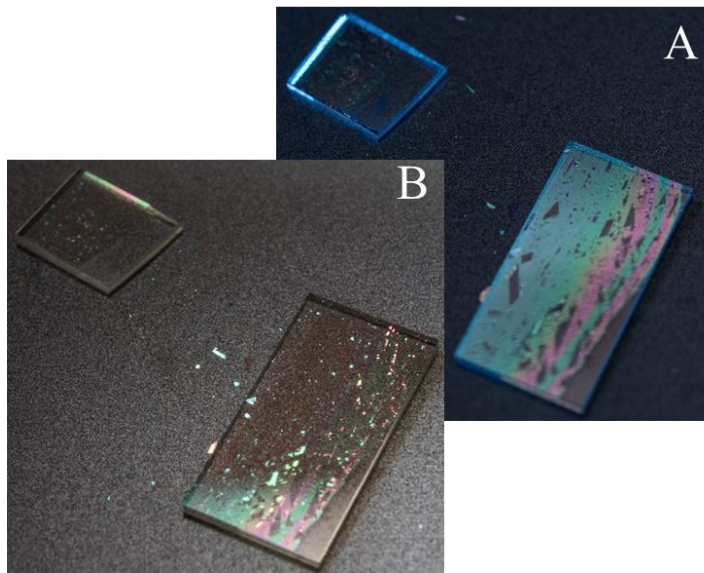


Figure 4.6 (A) Side and (B) front illumination of failed thin film LiNbO_3 sample.

These findings revealed that LPCVD was not a viable option for silicon nitride deposition on this particular material platform. Other options that were considered were sputtered silicon nitride and plasma enhanced CVD (PECVD) silicon nitride. While sputtered silicon nitride may have provided a closer stoichiometric match than PECVD silicon nitride, surface roughness, an issue inherent to sputtered films, may have proven to cause just as much loss as the hydrogenated silicon nitride from the PECVD processing [35], [36]. With this knowledge, PECVD became the method of deposition used for the remainder of the project, and tests began using the in-house system.

A battery of deposition tests were run on silicon test wafers as an alternative to using LiNbO_3 wafers initially to save on cost, also knowing that no crystallogical stresses would be added to the films with silicon nitride being amorphous. The gas chemistry for the deposition used was 10.0 sccm of silane (SiH_4),

6.0 sccm of ammonia (NH₃), and 300 sccm of nitrogen (N₂). The chamber was at a pressure of 100 Pa, the RF power was 60 W, and the platten temperature was set to 300° C. Depositing with multiple process times and measuring using an ellipsometer, a deposition time of 4 minutes and 28 seconds was determined to achieve the required film thickness of 200 nm.

While knowing the needed time of deposition, characterization of run-to-run index variation was pursued. In close succession, 3 samples were processed in the PECVD, and their index measured using the ellipsometer. The results of these measurements are shown in Table 4.1.

Table 4.1 Results of preliminary index variation inquiry.

Time (MM:SS)	Measured Thickness	Measured Index
4:28	<i>Sample 01</i> : 200.6 nm	1.980
	<i>Sample 02</i> : 195.9 nm	1.953
	<i>Sample 03</i> : 196.2 nm	1.945

The results show that 200 nm can be deposited within a 3% error margin on a bulk silicon substrate. However, from reviewing all the data collected during PECVD testing, it was found that index of the film could range from 1.88 to 2.00. This variation in index would result in the angle of the waveguides from the crystalline z-axis ranging from 69° to 80° for a thin film LiNbO₃ thickness of 600 nm. To allow for easier device prototyping, decreasing the index variation was desirable, as having granular waveguide angle control though 11° of variation is unwieldy. To mitigate this variation, it was found that purging the silane and ammonium lines to remove any stale and stagnant gas for 10 minutes prior to every deposition provided a much smaller index variation of 1.97 to 2.03. This smaller index range involved resultant in

waveguide angles needed between 69° and 71° , a more practical range of waveguides to have on hand.

4.3.2 Facet Polishing Development

In the current fabrication method, to obtain a testable device, dicing is required to create a facet that is perpendicular to the waveguides on the device. Dicing inherently adds chips and divots to the facet of the device, which makes coupling either inefficient or impossible. To mitigate the effects of dicing, mechanical polishing via lapping can be done. This is usually done by spinning a protective layer of resist onto the sample surface, mounting the sample perpendicular to a lapping disk, and using diamond grit pads to smooth and level out the facet to facilitate light coupling. The results from the perpendicular polish can be seen in Figure 4.7, which uses a proactive resist layer of NR9-3000P, spun to a thickness of $\sim 5 \mu\text{m}$, and baked at 120°C for 5 minutes.

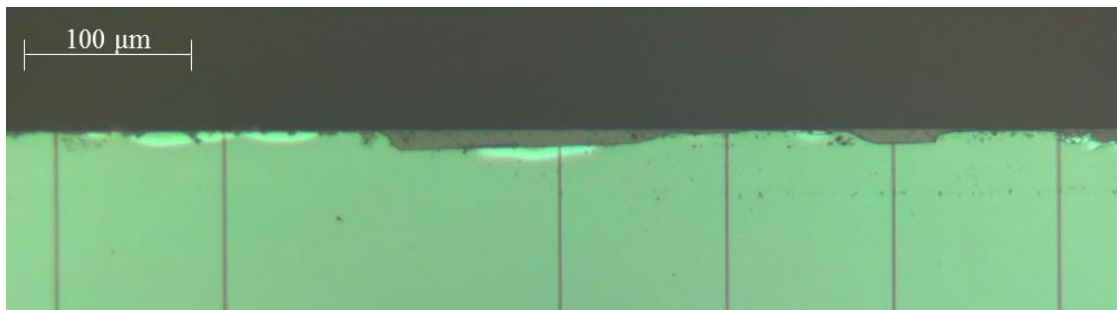


Figure 4.7 Chipping on surface after initial polishing.

As seen in Figure 4.7, even though chipping from the dicing saw was removed, chipping is introduced to the LiNbO_3 layer on top of the quartz. The current

theory behind this chipping is the hardness difference between LiNbO_3 (5H on the Moh scale) and quartz (7H on the Moh scale). To polish the quartz, a stronger downforce is needed than if just polishing LiNbO_3 alone. It is possible that the oxide-bonding layer between the LiNbO_3 and quartz layer is not robust enough to keep the LiNbO_3 attached to the quartz through the extra downforce needed, and this is something that cannot be controlled at this point in the process. However, there is a protective layer of resist that is added to the surface when polishing, and this could also be too soft and thin to absorb any shock the surface undergoes during polishing.

For the first attempt at solving this problem, a 45° mounting stub from a scanning electron microscope (SEM) was used. Using crystal bond (the bonding material used to hold the sample being polished to the chuck), the stub was attached to a compatible mount for the polisher, and the sample was then bonded to the top of the stub. The same protective layer of resist was used as in the previous case. Figure 4.8 shows the jig using the SEM stub, and Figure 4.9 shows the resulting facet from the polish.

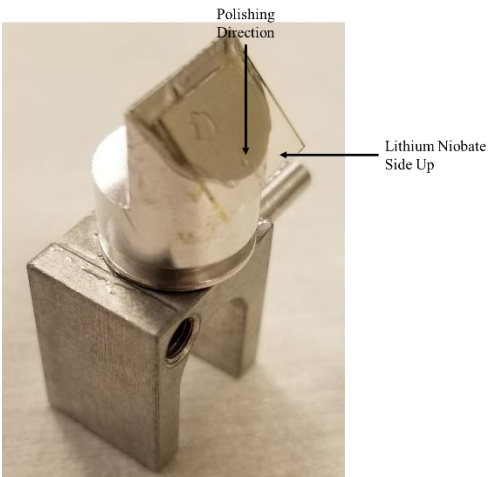


Figure 4.8 45° polishing jig using an SEM stub.



Figure 4.9 Resultant end facet after 45° polish.

This method proves to give an ideal facet with no visible chipping or divots. However, polishing at this angle would cause coupling issues since it is above the range of angles that satisfy total internal reflection. Due to the reflection, and therefore inability to couple into the device, this polishing method became the standard that the following methods were compared against for surface quality.

It was found that total internal reflection begins at approximately 30°, so a polishing jig was made to be approximately 15°, which was chosen to leave a large

margin of error for both creation of the mount and for pitch alignment error on the polishing system and the completed jig can be seen in Figure 4.10. Results from this jig are found in Figure 4.11.

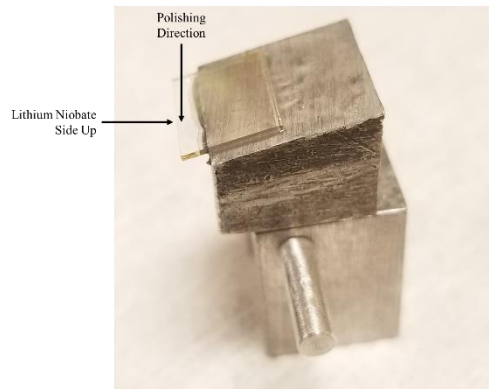


Figure 4.10 15° polishing jig.



Figure 4.11 Resultant end facet polishing at 15°.

While the chipping is still visible, it is less pronounced than in the first case (Figure 4.7). This improvement then lead to observing the effects of different permutations of protective coatings. The resist thickness was changed, the hardness of

the protective layer was varied, as well as using materials other than resist. Thickness was controlled by changing the type of resist used, and hardness was changed by increasing the amount of time the resist was baked on a hotplate after casting it on the sample surface. This increased baking time allows for more of the solvents to be removed from the polymers. Other materials that were used for protective layers were crystal bond, as well as another layer of quartz on top of the sample. Table 4.2 shows the varying materials and thicknesses that were used.

Table 4.2 List of materials and methods used for surface protection.

Material Used	Thickness	Bake Time	Polish Angle
NR9-3000P	5 μm	5 minutes	15°
NR9-3000P	5 μm	30 minutes	15°
Crystalbond	N/A	N/A	15°
Quartz bonded to surface with Crystalbond	N/A	N/A	0°
Quartz bonded to surface with NR9-3000P	N/A	N/A	0°
NR9-25000P	25 μm	45 minutes	15°

Most of the methods stated above provide improvement over the original sample, except for samples covered in crystal bond. It was found the crystal bond would chip off the surface during polishing and therefore offered little to no improvement to the surface of the chip. In Figure 4.12, a facet view (looking down onto the polished face) of the protective layers can be seen.

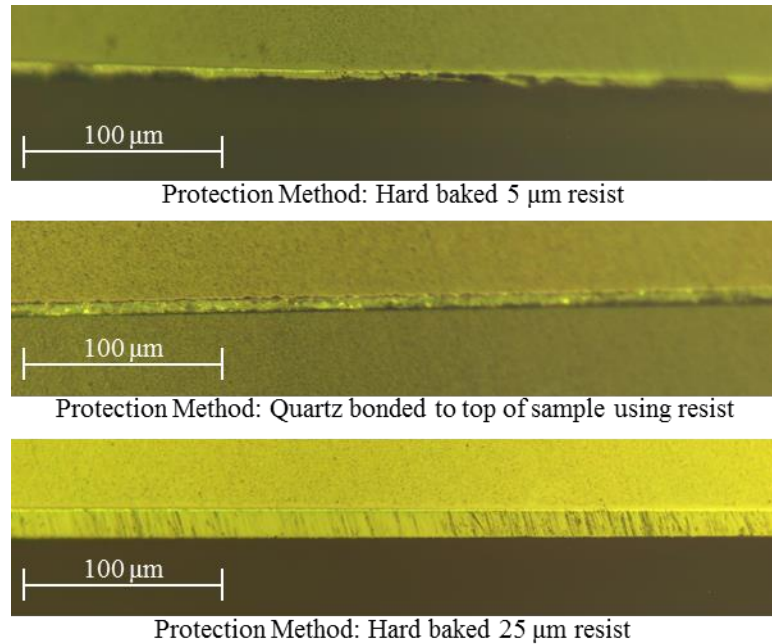


Figure 4.12 Facet view of protective layers after polishing.

The materials chosen to be viewed here offer a range of improvements from the original polishing method. It can be seen above that the hard baked, 25 μm resist offers the best method of protection from chipping. This is also evident while looking at the top surface after stripping the protective layer, which is shown in Figure 4.13.

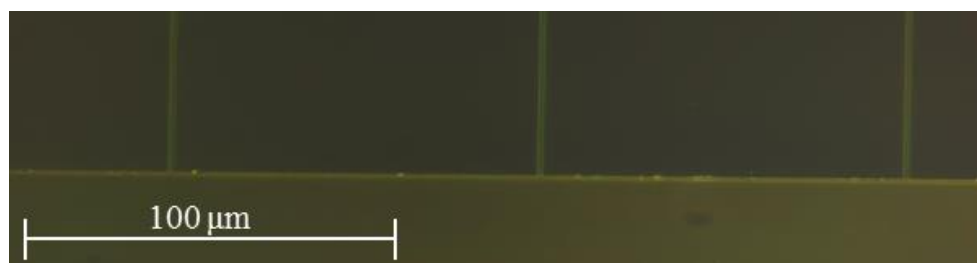


Figure 4.13 Dark field illuminated image post-polishing using hard baked, 25 μm resist.

While there was still some minor chipping evident, there were no areas of large chipping that covered most of the waveguides on the sample. Due to this improvement in facet quality, all samples developed were polished at a 15° angle using hard baked, 25 μm resist as the protective layer.

4.4 Waveguide Characterization

To confirm waveguide degeneracy, the same testing procedure to measure the FSR of the Ti:LiNbO₃ waveguides was performed, except with an added polarization splitter between the output fiber and the photodiode. This allowed the explicit capturing of the horizontal and vertical polarizations (the TE and TM modes of the waveguides, respectively) coming out of the device. Figure 4.14 shows the TE and TM launch into a 1.6 μm width waveguide.

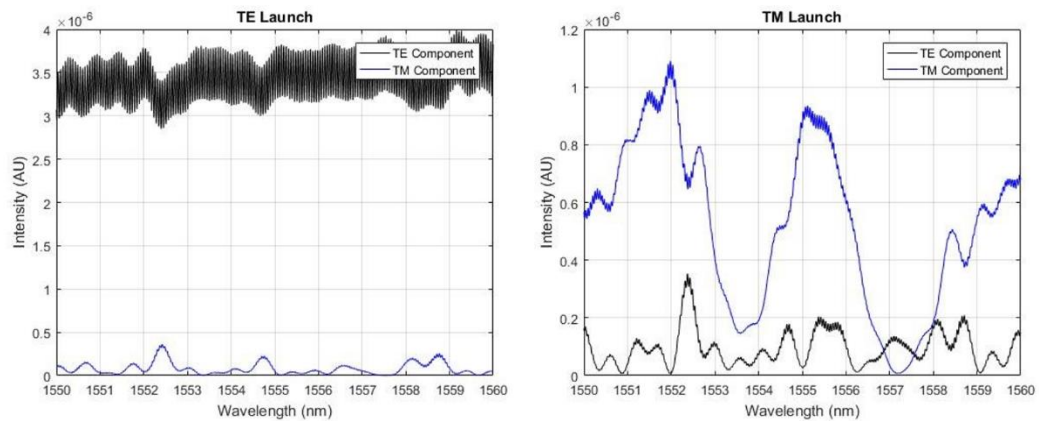


Figure 4.14 FSR response from TE and TM launched light in a silicon nitride ridge waveguide on thin film LiNbO₃.

In the TM launch case, the FSR response shows the normal, high spatial frequency sinusoid that is expected in a waveguiding cavity of this length. In the TE case however, the response shows minor indication of the typical sinusoidal response and is dominated by a much broader sinusoidal response, possibly caused by coupling irregularities invoked by a 15° facet due to polishing. The coupling differences between the orthogonal modes was observed by launching light with equal intensity between the TE and TM modes into a waveguide, and those results can be seen in Figure 4.15.

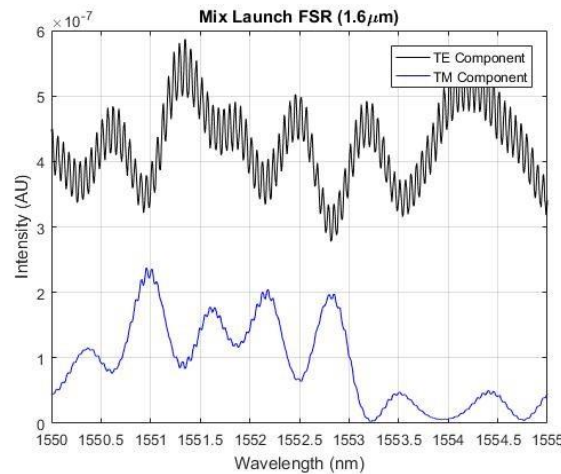


Figure 4.15 Mixed TE/TM launched light into a silicon nitride ridge waveguide on thin film LiNbO_3 .

Coupling into the device is apparently highly wavelength dependent, and as a result, a single wavelength was chosen for modulation response testing, which was 1552.83 nm, that offered the closest coupling between the two modes.

Since the modulation depth of the FSR for the TM signal was small, an alternate method of degenerate indication was used. The Fourier transform of a signal measured in units of wavenumber (nm^{-1}) will result in peaks that indicate resonances with respect to cavity length (in nm). The units of the recorded TE and TM FSR data were transformed into wavenumber, and the Fourier transform of the data was taken using the fast Fourier transform (FFT) function in MATLAB.

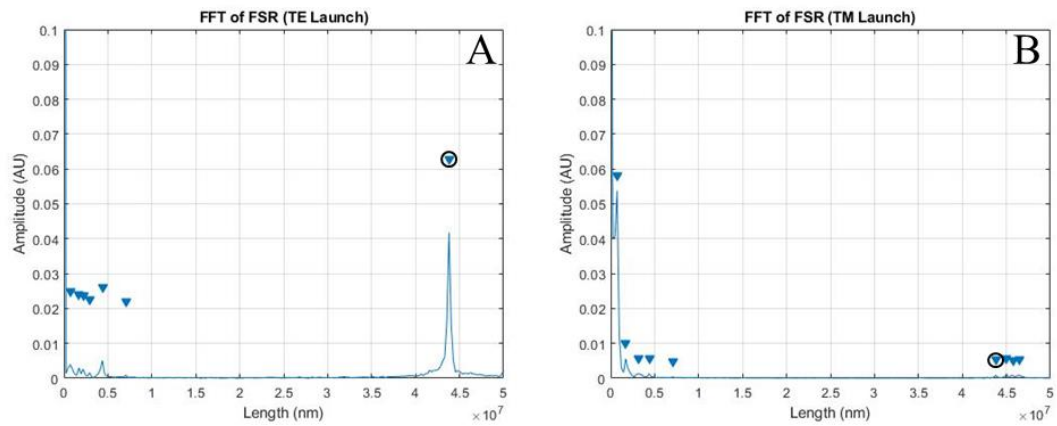


Figure 4.16 Fourier transform of FSR data of the TE (A) and TM (B) modes of the waveguide, with marked points of degeneracy.

In Figure 4.16, peaks around the effective cavity length of around 43.8 mm can be seen in each polarization, indicated by the circled markers. An effective cavity of this length corresponds to an effective index of around 2.19 in both modes. Although this index is higher than the simulated indices found in Section 4.2.2, the value is not unreasonable, and could be indication of the modes interacting less with the air cladding and silicon nitride rib and remaining more in the LiNbO_3 , which would provide better modulation efficiency during electrical perturbation.

4.5 Conclusion

In this section, silicon nitride is proven to be a viable method for creating a SLIQ-M. However, upon further comparison to a bulk Ti:LiNbO₃ platform, the thin film platform is theoretically expected to perform better. Due to its increased angle from the z -axis, when looking at the \mathbf{B} relation in Eq. (2.17), the thin film platform is calculated to have an effective EO coefficient of ~ 25 pm/V, while the bulk platform is ~ 1.4 pm/V. This improvement results in a much stronger response when samples are probed with vertical electric fields, which causes faster polarization rotation and will allow for a shorter device length. A depiction of this improvement is shown in Figure 4.17, where the same theoretical electric field is applied to each platform and the thin film device exhibits a larger deformed ellipse. This phenomenon is made evident in the testing to come in the following chapter.

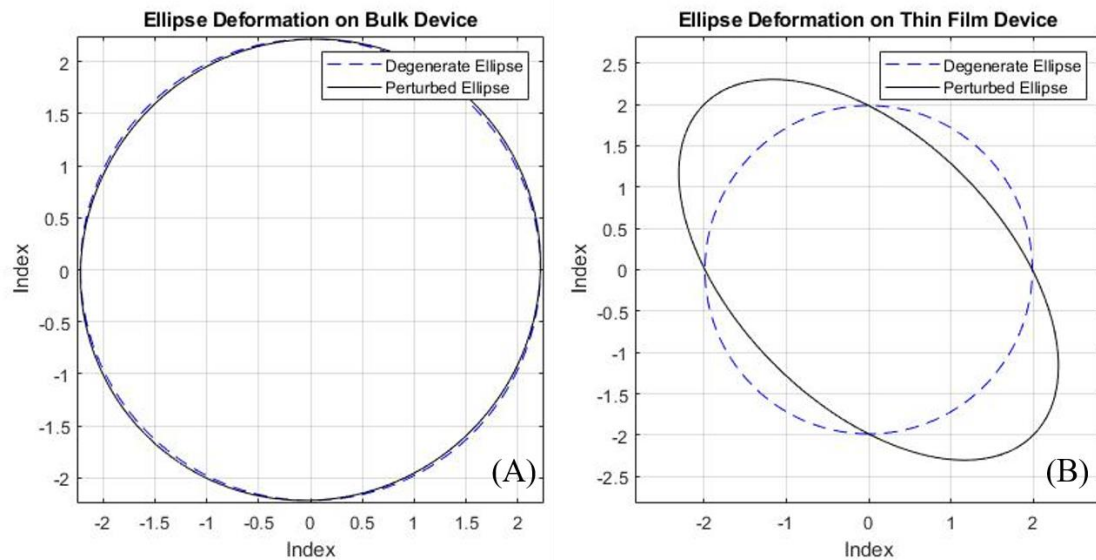


Figure 4.17 Theoretical improvement in ellipse deformation in A) bulk LiNbO₃ and B) thin film LiNbO₃.

Chapter 5

DC AND RF MODULATION TESTING

5.1 DC Testing

For DC analysis, electrode design is greatly simplified due to the laxed requirement for velocity matching required from high speed, traveling wave modulation [37]–[39]. However, electrodes still have a proximity tolerance such that the electric field travels through the optical mode with sufficient intensity and does not “short” between the electrodes. Having considered those constraints, a design was made such that the vertical and horizontal components of the EO tensor could be probed. This requires the use of a four-electrode design of ground-signal-signal-ground (GSSG). A depiction of what the resultant electric fields would look from such a design like can be seen in Figure 5.1.

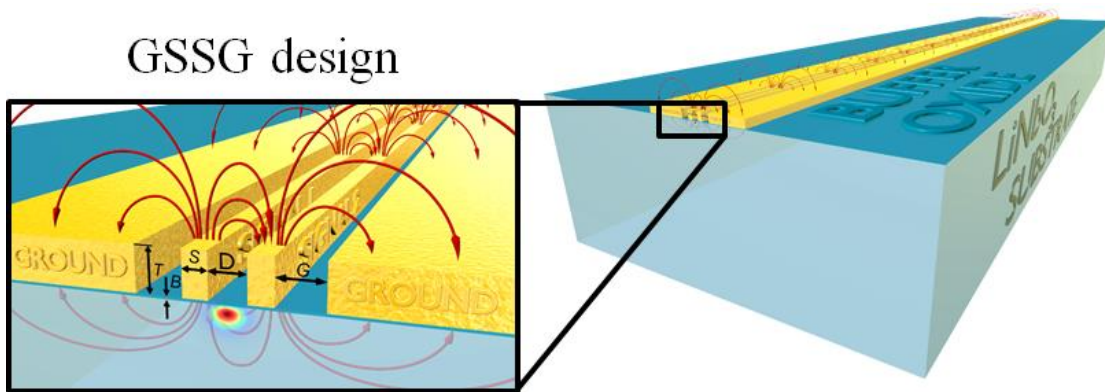


Figure 5.1 Depiction of E-fields in GSSG electrode.

Electrodes were 10 μm wide with probing pads at the end. The center to center gap between the two signal electrodes was 30 μm and the center to center gap from the signal to ground electrodes was 70 μm . These electrodes were fabricated using conventional contact lithographical techniques to pattern resist for liftoff, electron beam evaporation for metal deposition, and liftoff to leave the metal traces. The electrodes were 120 nm thick, with 20 nm of Ti to act as an adhesion layer and 100 nm of gold. The resulting electrodes can be seen on a bulk Ti:LiNbO₃ sample in Figure 5.2.

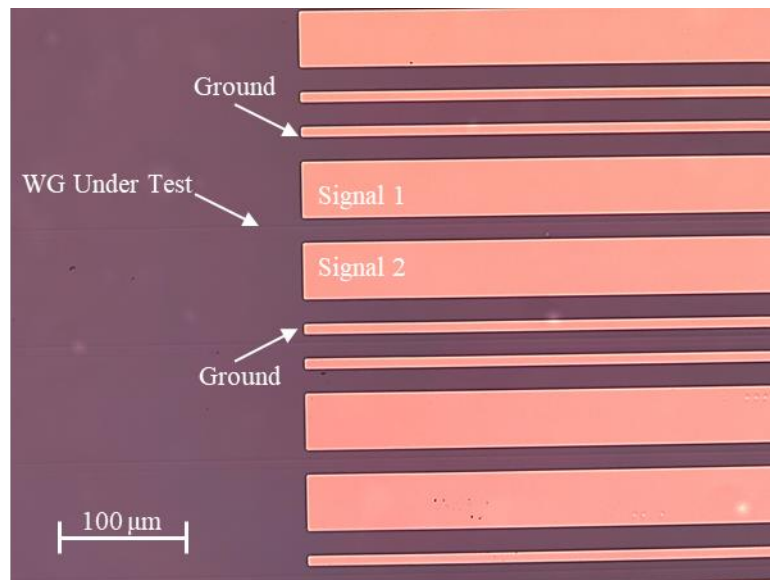


Figure 5.2 GSSG electrodes on a bulk Ti:LiNbO₃ sample.

To test the modulators, the samples was placed between two polarization maintaining (PM) lensed fibers to couple light in and out of the waveguides. These fibers had their slow axis aligned to TM mode such that the integrity of the input and

output polarizations are maintained during detection. The light is supplied by a 1550 nm laser and is passed through a polarization controller. The polarization controller consists of a vertical polarizer and a half wave plate. The vertical polarizer is to ensure that the light going into the half wave plate is vertical (or TM, the orientation of the slow axis of the PM fiber) and helps mitigate any polarization drift the laser may experience. The half waveplate is rotated to give TE (horizontal), TM (vertical), or any desired angle of linearly polarized light. After the lensed fiber used for collection, a polarization splitter separates the fast and slow axis (e.g. vertical and horizontal polarizations) of the fiber so they can each illuminate a different InGaAs photodetector. The output of each photo-detector is sent to a transimpedance amplifier (TIA) so the photodiode current can be amplified and mapped to a voltage. The output from the two TIAs is then routed to an oscilloscope so the voltage signals can be recorded. A dual-channel function generator supplies the electrical input through needle probes to the respective components of the electrodes. The needle probes, lenses fibers, sample stage, and sample are seen in Figure 5.3.

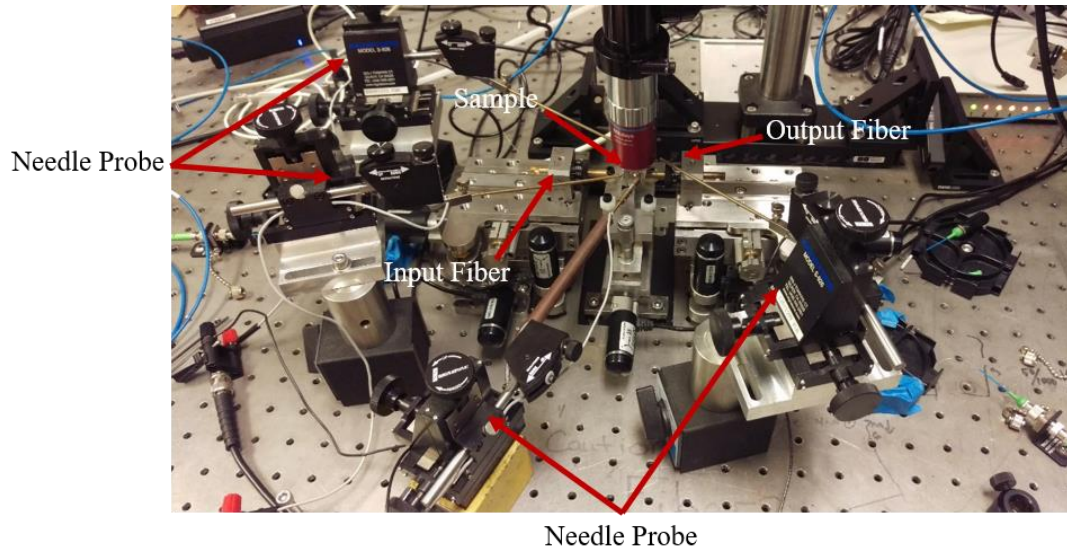


Figure 5.3 DC measurement test set-up showing input fibers and output fibers, needle probes, and sample under test.

For a given waveguide, light was launched in TE, TM, and a hybrid (45° between TE and TM) polarizations. For electrical stimuli, three variations of a $10 V_{pp}$, 1 kHz dual triangular wave input were used. One signal consisted of the triangle waves being in phase (0° relative offset), one with the triangular waves 180° out of phase, and the final with the waves being 90° out of phase. The signal with the in-phase waves is to perturb the modulator such that electric field is vertical and causes polarization rotation, while the 180° out-of-phase signal is to create horizontal electric fields responsible for causing phase modulation. These phenomenon are visualized in Figure 5.4, based off the theoretical response of the index ellipse, calculated in Eq. (2.17). Each variation of the input polarization was subject to each variation of the electrical stimuli.

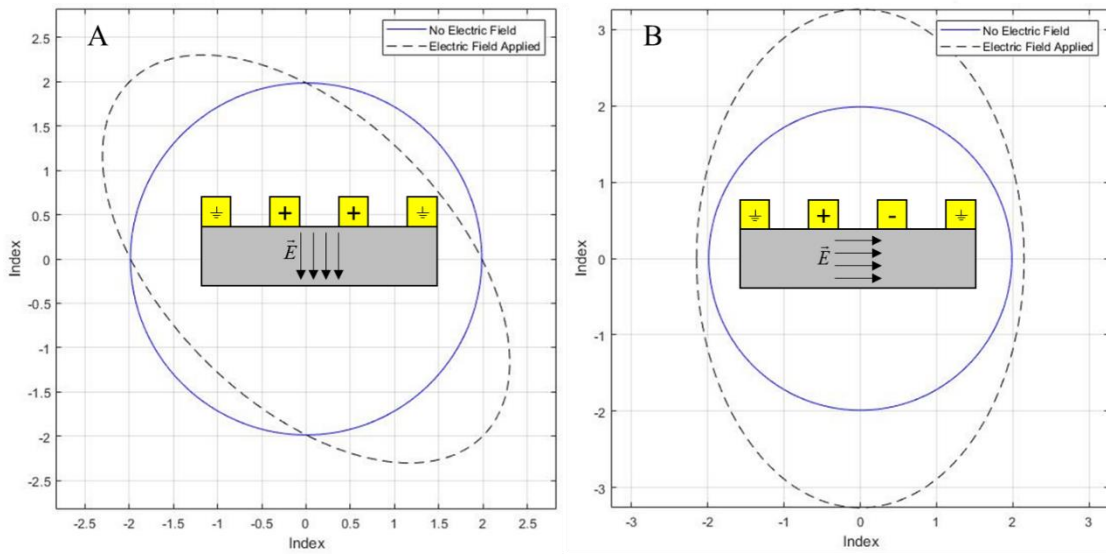


Figure 5.4 Visualization of changing index ellipse from electric fields in the (A) vertical and (B) horizontal direction with respect to the sample surface.

5.1.1 DC Results from Ti:LiNbO₃ platform

With the voltages available from the function generator supplying the electric signals, significant modulation in the Ti:LiNbO₃ platform could not be seen without filtering. Using the built in filters on the TIA, a high pass filter with a cut-off frequency of 3 Hz with a 12 dB per octave roll-off was used. The result of launching TM (vertical) light through the waveguide with a 0° offset of the electrical stimuli is shown in Figure 5.5 and the results of launching TE (horizontal) light through the waveguide with 180° offset of the electrical stimuli is shown in Figure 5.6.

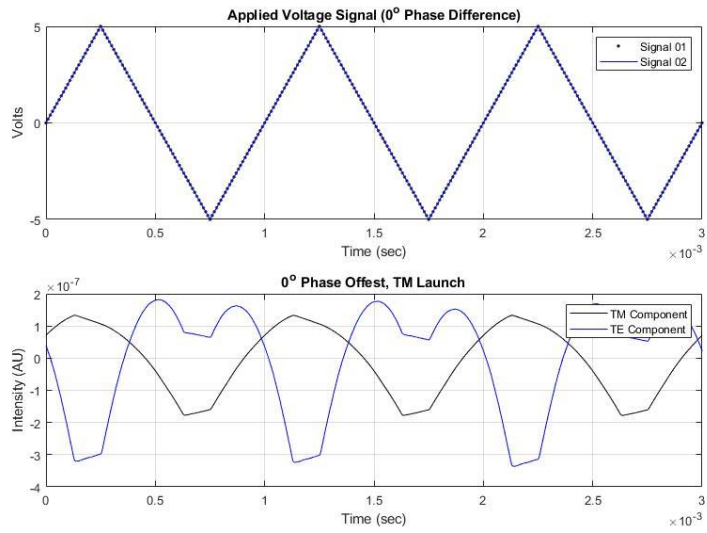


Figure 5.5 Results of in phase signals with TM polarized light launch in bulk Ti:LiNbO₃ platform.

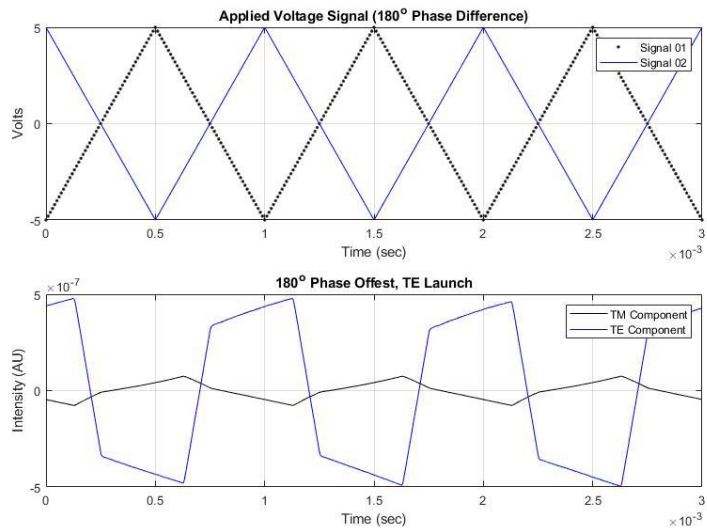


Figure 5.6 Results of out of phase signals with TE polarized light launch in bulk Ti:LiNbO₃ platform.

The first issue of note is the intensities of the response of each recorded signal. If the phenomena of ellipse morphing is occurring as depicted in Figure 5.4, there should be more polarization change evident in the perturbation case of Figure 5.5 than in Figure 5.6. A possible reason for this difference is the overlap of the electrical and optical mode. In the case of vertical electric field perturbation, the electric field lines are not swelling far enough between the two signal electrodes to have a significant effect on the optical signal, while in the horizontal perturbation case there is a much stronger overlap and, therefore, a larger response. However, polarization rotation is still believed to be happening in Figure 5.5 as expected, due to the sinusoidal nature of the response, which would be expected of an oscillating phenomenon. The anomalies in that signal could also be explained by a parasitic capacitance somewhere in the device and a change in the FSR due to the experienced change of index. The observed polarization rotation in Figure 5.6, which is not expected, is explained by the nature of the degenerate waveguides. If the waveguide is truly degenerate, any kind of perturbation, be it physical (waveguide defects) or thermal (temperature gradients) imperfection, could cause the index ellipse to lose degeneracy, but electric field “defects” would also cause this to happen. Electric field “defects” are being referred to here as an electric field that is not perfectly horizontal through the optical mode, and there is high probability that this is the case. Knowing that vertical electric fields cause polarization rotation, this explanation becomes likely. So, albeit not effective, using the knowledge of the construction of the device, the Ti:LiNbO₃ platform would be viable as a vector modulator with an improved electrode structure. However, it will be found in the next section that the silicon nitride rib platform is more effective.

5.1.2 DC Results from Thin-Film LiNbO₃ Platform

As was the case in measuring the response from the Ti:LiNbO₃ platform, for closer inspection of the effects of the electric stimuli of the device, filtering from the TIA was needed. However, unlike the previous platform, a non-DC signal response was able to be viewed and recorded and is seen in Figure 5.7. Figure 5.8 shows the filtered response of TE light being launched into the device with in-phase electrical stimuli being applied, and Figure 5.9 depicts the response of TM light being launched into the device with out-of-phase electrical stimuli being applied, all on 1.6 μm wide waveguides.

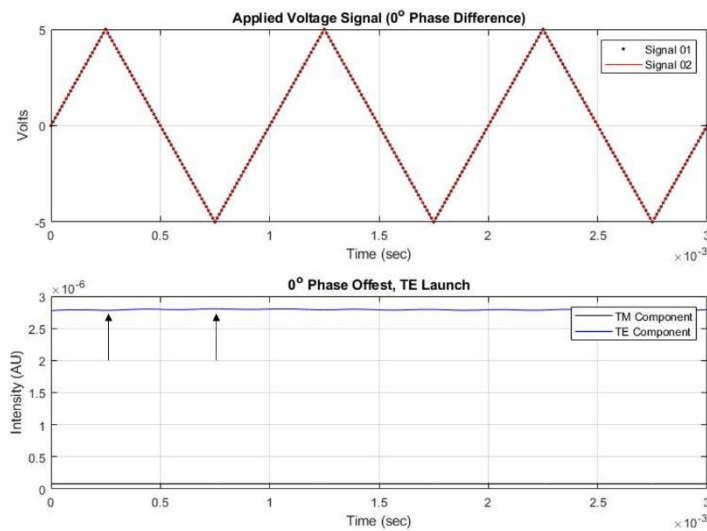


Figure 5.7 Unfiltered response of TE launched light with in-phase electrical stimuli on a thin film LiNbO₃ device.

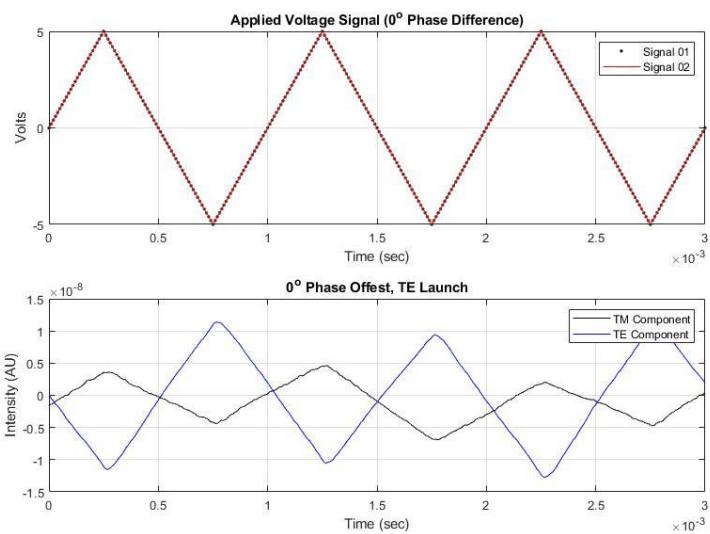


Figure 5.8 Filtered results of in-phase signal with TE launched light on a thin film LiNbO_3 device.

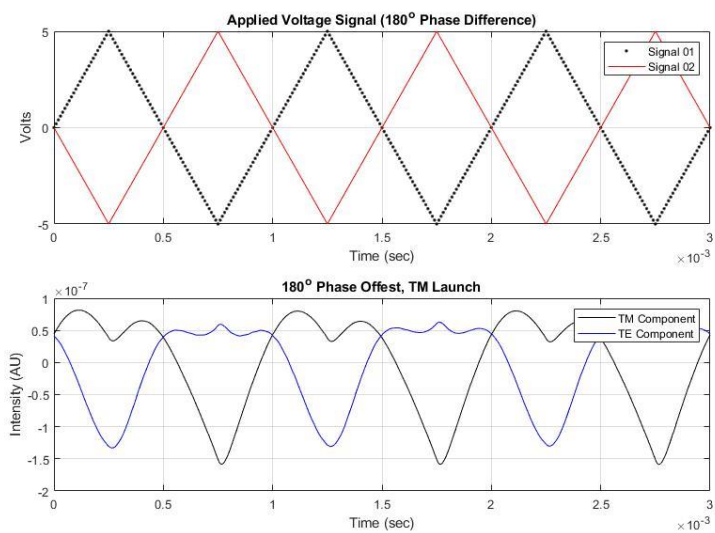


Figure 5.9 Filtered results of out-of-phase signal with TM launched light on a thin film LiNbO_3 device.

It can be seen that these test results most likely suffer from the same issue that the Ti:LiNbO_3 test does: mode overlap. The issue is further exacerbated by the optical mode being much smaller in the thin film variation of the device (approximately $2\ \mu\text{m}$ in diameter, see Figure 4.5) than the bulk variation (approximately $8\ \mu\text{m}$ in diameter, see Figure 3.2). Despite the disadvantage of even less mode overlap, the thin film platform shows improvement over the bulk Ti:LiNbO_3 platform qualitatively by polarization being evident even when the device response is not filtered. This is shown even more evidently in Figure 5.10, where light was launched with even intensity between the TE and TM into a thin film device, and excited by 90° offset signals, a means of probing both phase modulation and polarization rotation.

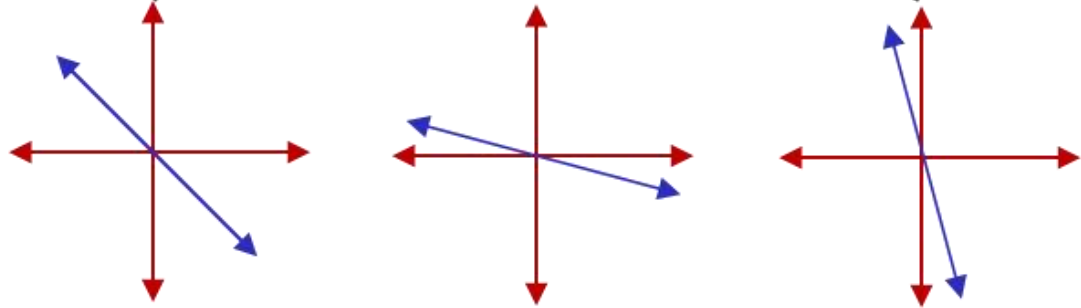
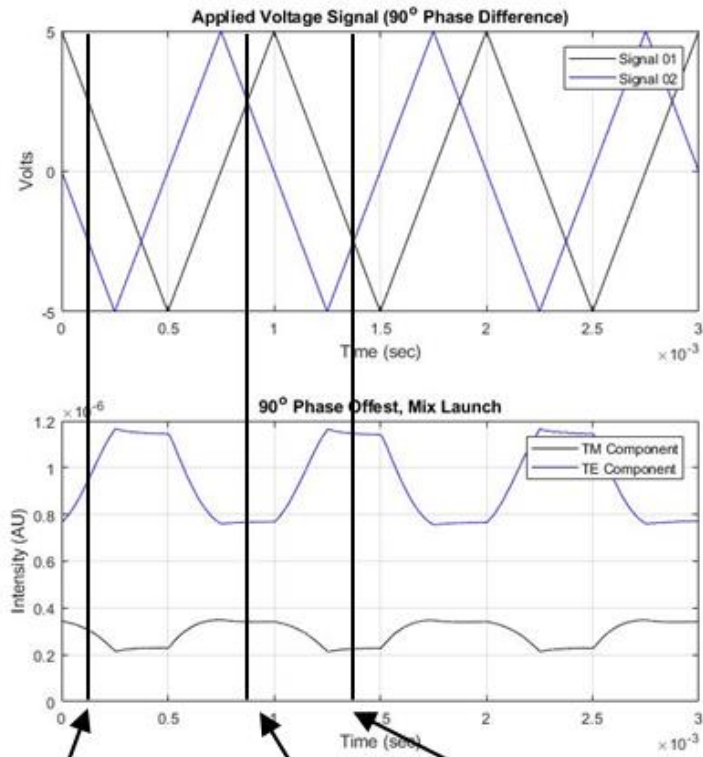


Figure 5.10 Mixed TE/TM optical launch with 90° offset signals on a thin film LiNbO₃ device.

5.2 RF Characterization

Having viewed the device functions under DC excitation, the next step taken was to test the devices at higher frequencies. A new set of electrodes needed to be designed to complete the higher frequency tests. The previous samples used for DC testing could not be used as the electrode traces were too thin and their spacing did not match any GSSG probes that could be purchased. The electrodes were designed to match with a GSSG probe that has tip spacing of 100 μm center-to-center. For the devices made for this testing, the interaction region is 8 mm long. The short length means that, at the highest frequency that could be tested (10 GHz), the device would still operate in lumped conditions since the wavelength of 10 GHz (3 cm) is over three times the length of the device length. This operational mode simplifies the design, as velocity matching is not necessary in devices that operate in lumped conditions.

Despite this simplification, impedance matching for maximum power transfer and minimal reflections in the RF feed system is still required. In the case of a 50 Ω feed system, a conventional GSG system would need an impedance of 50 Ω , as one coaxial cable would feed the probe. However, in the case of using GSSG electrodes, the probe is fed with two coaxial cables, and a depiction of this is shown in Figure 5.11.

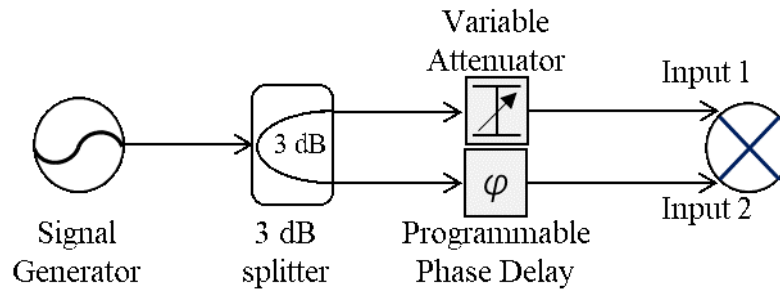


Figure 5.11 RF feed path to drive tested devices.

Explanation of the components used in the feed path will be confounded upon shortly. To further complicate the impedance matching, the device operation can be broken down into two modes: when input 1 and input 2 are in phase, and when they are out of phase. These two modes of operation result in an equivalent circuit representation that look as follows:

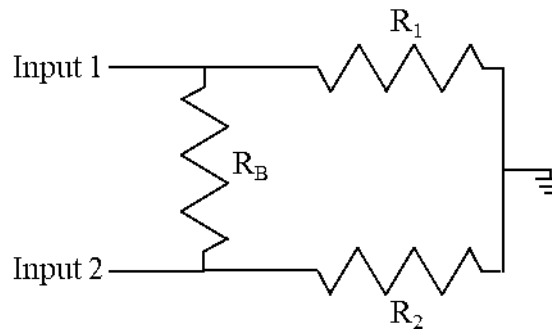


Figure 5.12 Equivalent circuit representation of the RF operation on the device.

The equivalent resistances of the signal paths through the device are

$$\begin{aligned}
(\textit{Case 1}) R_{total} &= R_1 \parallel R_2 \\
(\textit{Case 2}) R_{total} &= R_B \parallel (R_1 + R_2),
\end{aligned}
\tag{5.1}$$

where *Case 1* occurs during in phase operation, and *Case 2* occurs during out of phase operation. Knowing that each input is fed by a 50 Ω line, R_1 and R_2 must have an impedance of 50 Ω , meaning R_{total} has a value of 25 Ω for *Case 1*. This means that R_B must have an impedance of 33 Ω in order to maintain the same impedance in both operation cases. For some optimization, Ansoft's HFSS was used to determine the parameters of the electrodes. In this iteration, a minimum impedance of 75 Ω was achieved using a design that consisted of 400 nm thick electrodes, with an electrode width of 80 μm , signal-to-ground separation of 30 μm , and a signal-to-signal separation of 12 μm . This can be visualized in Figure 5.13, showing the electrodes on a thin film LiNbO_3 device. The electrodes were fabricated using conventional contact UV lithography, electron beam evaporation of a 50 nm Ti adhesion layer and 350 nm layer of gold, and liftoff techniques to leave the electrode traces.

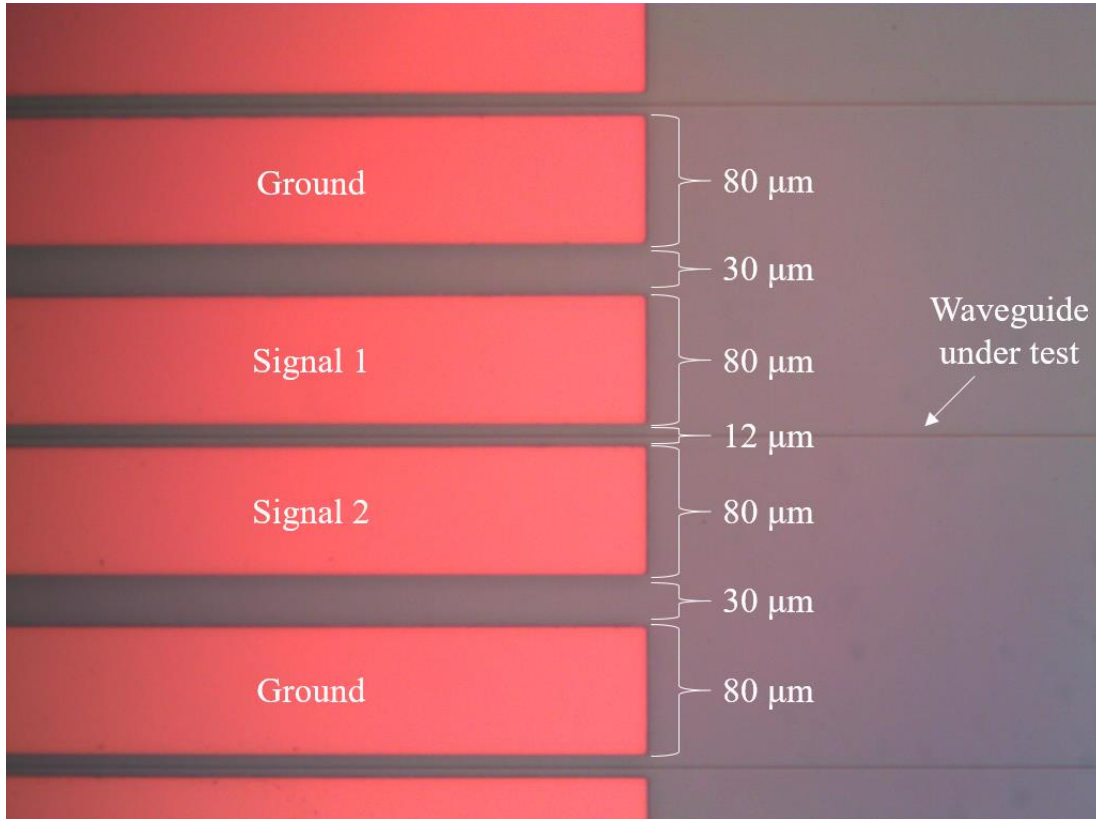


Figure 5.13 High frequency electrodes on a thin film LiNbO₃ device.

With the theoretical and observed performance of the thin-film LiNbO₃ device over the Ti:LiNbO₃ device, RF testing was only on the previous platform.

5.2.1 RF and Optical Signal Paths

As shown in Figure 5.11, the RF feed uses a signal generator, a 3 dB splitter, a digital phase shifter, and a digital attenuator. Using a 3 dB splitter from one signal generator removes the need for two signal generators to create the dual signal RF feed. Using two signal generators would require extensive calibration to ensure they are locked in relative phase with each other. The digital phase shifter used has

360° of phase control, which is required to find the point of phase coherence between the two legs, and then be able to shift the phase of one leg by 180°. The digital attenuator is used to match the power traveling down each leg since the phase shifter has a non-zero insertion loss.

To calibrate the phase of the feed, Input 1 and Input 2 were combined into a single RF detector, and the digital phase shifter was adjusted to find the point of highest extinction between two signals. This marked the 180° phase shift between the signals, and 180° was subtracted from the value to find the in-phase adjustment. To adjust the digital attenuator, the power from each leg was measured individually, and the attenuator was adjusted to match the power of the phase shifting leg.

To launch and collect the light to and from the device, the setup flow depicted in Figure 5.14 was used.

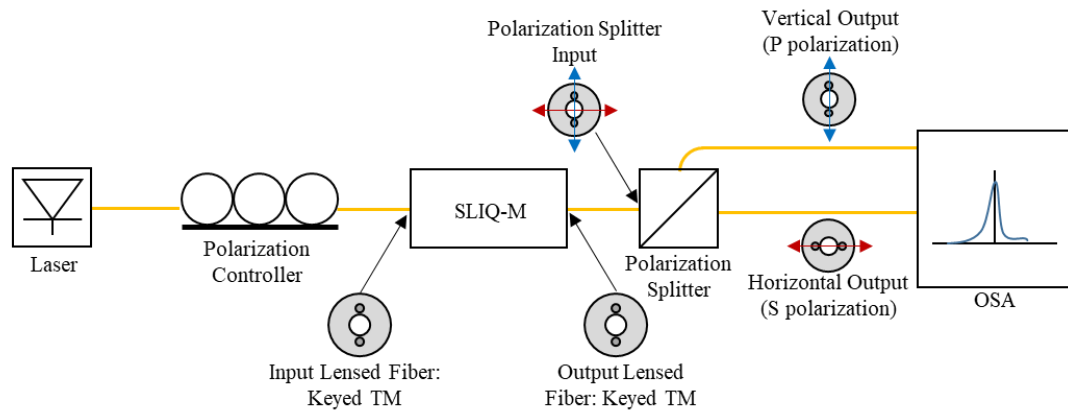


Figure 5.14 Optical components and signal flow used for device measurement.

The system was excited with a tunable laser that fed into a polarization controller. The polarization controller consisted of a vertical polarizer followed by a rotating half

wave plate. The light then fed into a PM lensed fiber, keyed such that the slow axis was oriented in the p -plane of the device. After coupling into the device, the light was collected on another p -keyed PM lensed fiber. The signal was then split using an in-fiber polarization splitter to separate the slow (p -polarization) and fast (s -polarization) axis of the fiber so that each polarization could be individually recorded with an optical spectrum analyzer (OSA).

5.2.2 Experimental RF Results

The device was excited with a -13 dBm 4 GHz RF signal with relative phases between each signal leg being 0° , 90° , and 180° as to probe responses from vertical fields, horizontal fields, and a mix between the two. To record the response of the device in each case, the data was collected from one leg of the polarization splitter at a time, as the OSA only has one input port. Figures 5.15 and 5.16 show the raw collected response of TE and TM launched light, respectively, and Figure 5.17 shows the normalized response of TE launched light with annotations on the sidebands for closer analysis.

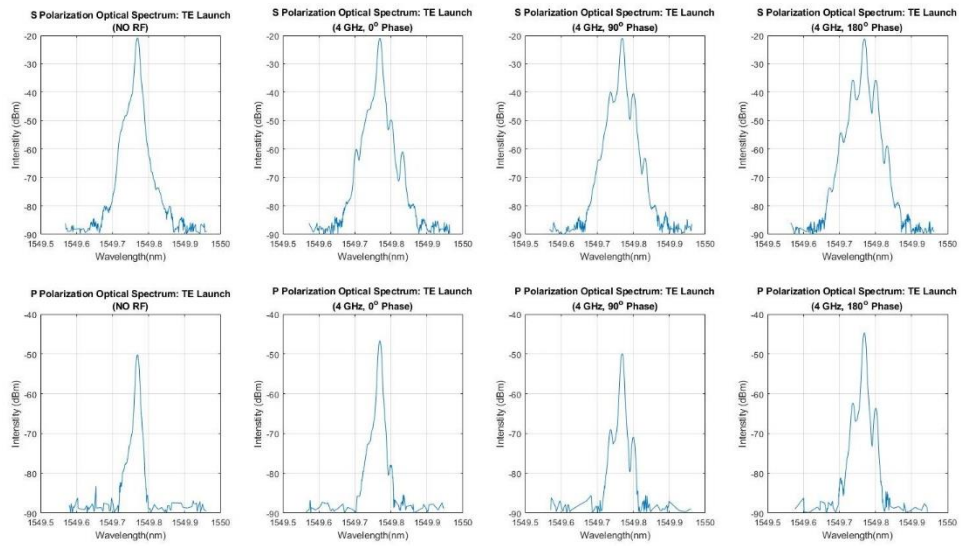


Figure 5.15 Collected data from TE launched light into a thin film LiNbO_3 device with 4 GHz excitation.

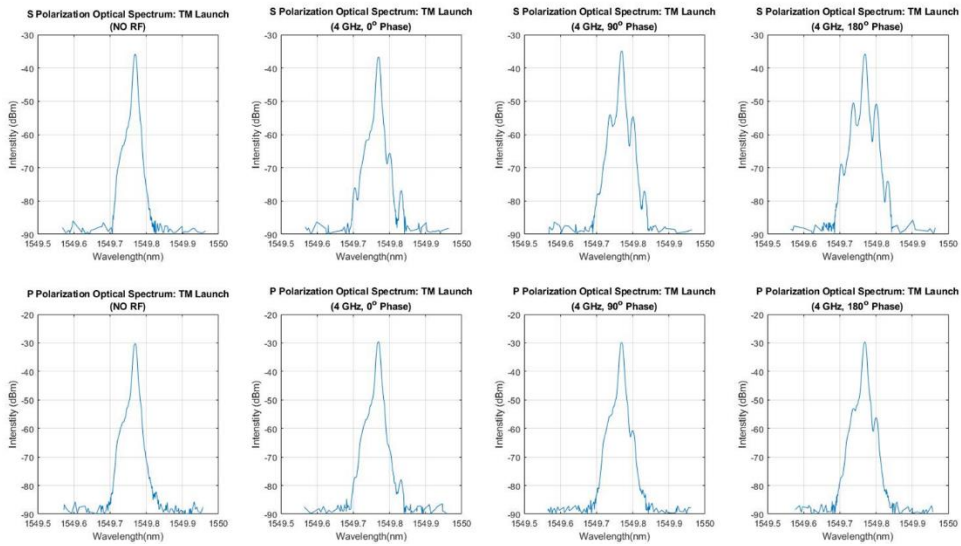


Figure 5.16 Collected data from TM launched light into a thin film LiNbO_3 device with 4 GHz excitation.

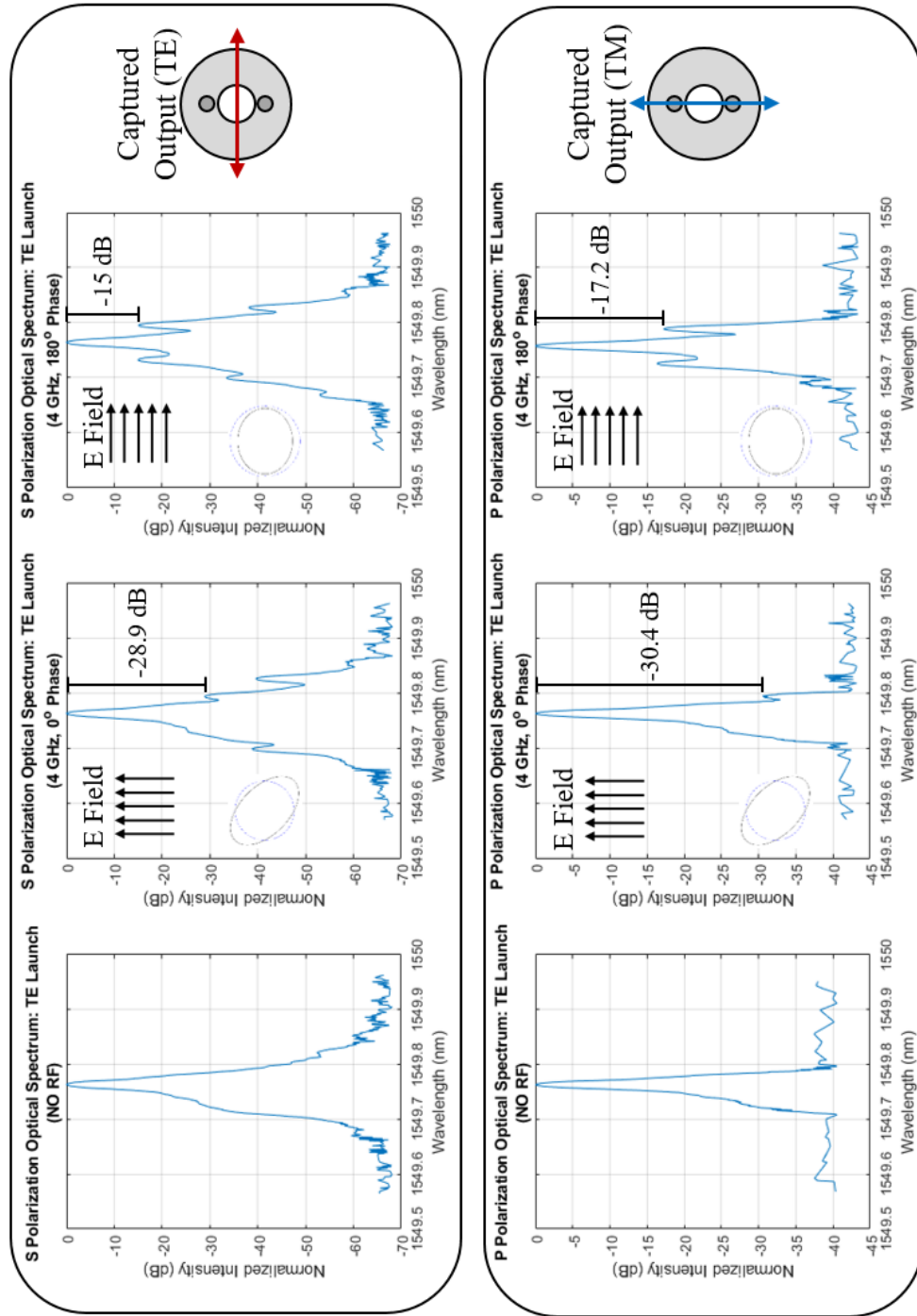


Figure 5.17 Normalized response of thin film LiNbO₃ at 4 GHz excitation.

It can be seen that side bands occur at each phase offset of the RF, indication of modulation. The asymmetry of the response should be noted. This is predicted to be due to the impulse response of the OSA. Since the carrier is recorded asymmetrically, any side bands that appear become convolved with the carrier response, and, therefore, would appear asymmetrical as well. For the *s* collected polarization case in Figure 5.14, the carrier appears at a wavelength of 1549.7640 nm, with first order sidebands at 1549.7336 nm and 1549.7944 nm and second order sidebands at 1549.6992 nm and 1549.8264 nm. This spacing corresponds to a 4 GHz signal, and holds true for every instance recorded. Also, the sideband amplitude is not equal in every case. This can be explained by difference in RF mode overlap in each of the operation cases (a weaker overlap at 0° offset and stronger overlap at 180°), and by differing values of the effect EO coefficients for each offset case. It is also worth noting the ratio of the sidebands are not the expected values. For the 0° phase case, the difference between the TE and TM side bands should be 0 dB, since the change from degeneracy caused by this electrical perturbation is the same for both modes. For the 180° phase case, the difference between the TE and TM sidebands should be approximately 4 dB, the ratio of the change from degeneracy in both modes. These difference are explained by the differences in mode confinement in the LiNbO₃. For the TE and TM modes, different amounts of light remain in the LiNbO₃, which effects the modulation efficiency of the device.

When looking at the different carrier only signals recorded by the OSA, in the case of TE launch, an extinction between the recorded TE and TM signals of about 30 dB is realized. However, when observing the TM launched signals, an extinction of 10 dB is shown. The theory for this difference in extinction is a 10 dB reduction in coupling in the TM mode versus the TE mode. This is due to the facets not being perpendicular to the optical axis (discussed in Section 4.3.2). If this is accounted for, an extinction of 20 dB would occur between both modes, which is the maximum extinction that the polarization controller offers, limited by human error (tuned by hand), and the specifications of the elements that compose the controller.

5.3 Conclusion

The electrical testing done on these devices prove that the SLIQ-M concept is a viable modulator architecture to achieve vector modulation. The bulk and thin-film LiNbO₃ platforms are tested, and the previously predicted benefits of using thin-film LiNbO₃ are confirmed to be true. Although shown to be functional at higher frequencies, there are still obstacles to overcome in coupling, RF and optical mode overlap, and electrode impedance that limit the effectiveness of the current modulator design. Improvement in these areas are expanded upon in the final chapter.

Chapter 6

CONCLUSION

6.1 Summary

In this work, a concept for a single line IQ modulator is presented as an alternative to using off-the-shelf parts to achieve vector modulation. Operation of single line IQ modulation is derived and simulated, the platforms of bulk LiNbO₃ using Ti diffused waveguides and thin-film LiNbO₃ using rib structures were introduced, and their viability and effectiveness postulated. Devices using both the bulk Ti:LiNbO₃ waveguide platform and thin film LiNbO₃ with silicon nitride rib waveguide platforms were successfully fabricated. Each platform was tested under DC excitation. After being found that thin-film LiNbO₃ was more effective, it was tested at 4 GHz. The devices showed varying responses for different excitations, indication of different morphing of the index ellipse, as expected from the theoretical calculations.

6.2 Future Work

Future progression of this research will focus on device improvements and increased theoretical understanding of operation. First, the device will benefit greatly from improvement to facet polishing. Physically, finding a method to effectively polish facets perpendicular to the waveguiding axis would increase the coupling efficiency and remove the ~10 dB difference between TE and TM modes. A proposed method would be to use plasma etching. The sample would have a mask fabricated on it such that it covers all but the edges of the sample. An ICP-RIE etch tool would be used to etch through the exposed LiNbO₃, leaving a flat sidewall against the mask.

Finally, the mask would be stripped. Figure 6.1 depicts a theoretical process flow for accomplishing this.

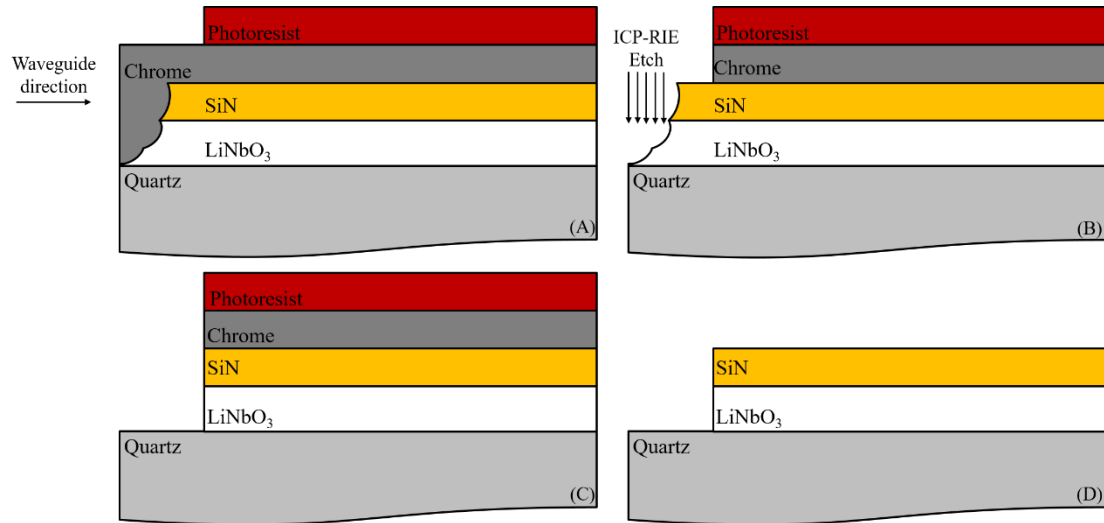


Figure 6.1 Proposed facet etching fabrication flow. (A) Coat sample in chrome and cover with resist; (B) etch back chrome to expose damaged device layer and etch using an ICP-RIE resulting in (C); (D) remove chrome and resist masks.

This method of removing damage removes the need to mechanically polish, which could possibly require material bonding to offer the needed protection required to prevent device layer chipping.

The device also requires properly designed electrodes for effective RF power delivery. Mode simulations can be done using HFSS to determine the ideal dimensions of the electrode for maximum mode overlap and optimize the impedance along the electrodes, which is known from Section 5.2. However, when coupling RF energy into the system, if a $50\ \Omega$ probe pad is developed with an adiabatic taper to

match the impedance, the electrode impedance can be separated from the electrode impedance throughout the rest of the device. Depiction of such a design is shown in Figure 6.2

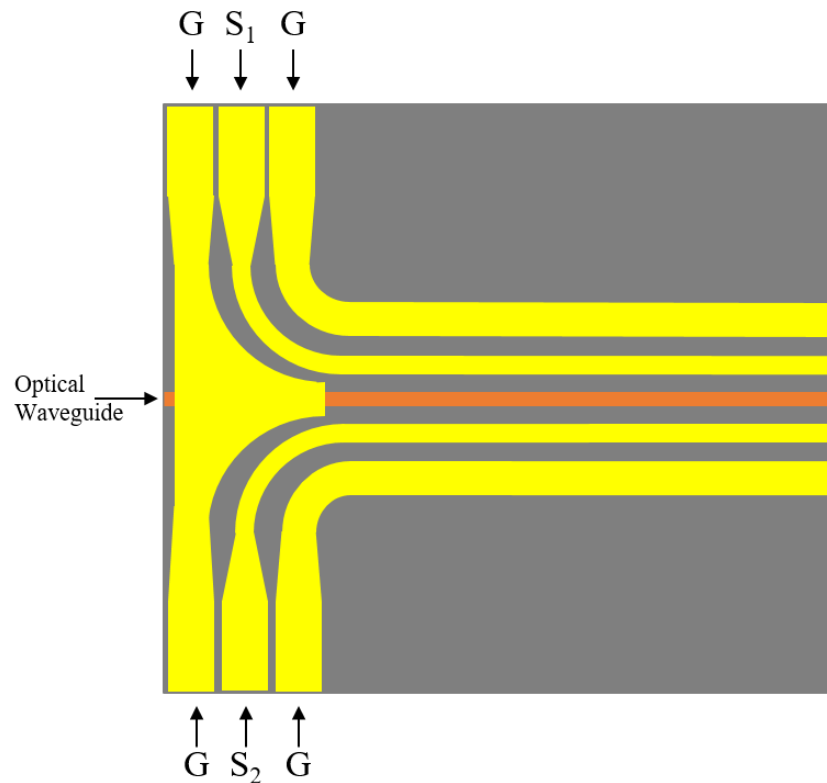


Figure 6.2 Split GSSG electrode concept.

Finally, improvements in the deposition process for the silicon nitride rib can be pursued. Mitigation of the loss caused by extra hydrogen in the material would allow longer devices to be made with similar throughput capabilities. Improvement in all of these areas would elevate the performance of a SLIQ modulator.

REFERENCES

- [1] B. Saleh and M. C. Teich, *Fundamentals of Photonics*, Second. Wiley, 2007.
- [2] S. Abbott, “Review of 20 years of undersea optical fiber transmission system development and deployment since TAT-8,” in *2008 34th European Conference on Optical Communication*, 2008, pp. 1–4.
- [3] “FCC Promotes Higher Frequency Spectrum for Future Wireless Technology,” *Federal Communications Commission*, 22-Oct-2015. [Online]. Available: <https://www.fcc.gov/document/fcc-promotes-higher-frequency-spectrum-future-wireless-technology>. [Accessed: 15-Nov-2018].
- [4] G. C. Tavik *et al.*, “The advanced multifunction RF concept,” *IEEE Trans. Microw. Theory Tech.*, vol. 53, no. 3, pp. 1009–1020, Mar. 2005.
- [5] M. Marcus and B. Pattan, “Millimeter wave propagation: spectrum management implications,” *IEEE Microw. Mag.*, vol. 6, no. 2, pp. 54–62, Jun. 2005.
- [6] FCC, “Millimeter Wave Propagation: Spectrum Management Implications.” Federal Communications Commission, Jul-1997.
- [7] X. Ge, S. Tu, G. Mao, C. Wang, and T. Han, “5G Ultra-Dense Cellular Networks,” *IEEE Wirel. Commun.*, vol. 23, no. 1, pp. 72–79, Feb. 2016.
- [8] “Ever wonder how much a fiber or Ethernet cable weigh?,” *Myriad Supply Blog*, 05-Dec-2011. [Online]. Available: <https://www.myriadsupply.com/blog/ever-wonder-how-much-a-fiber-or-ethernet-cable-weight/>. [Accessed: 15-Nov-2018].
- [9] Andrew Corperation, “HELIX Coaxial Cable; Insallaion Instructions.” Andrew Corperation, 1998.
- [10] G. J. Schneider, J. A. Murakowski, C. A. Schuetz, S. Shi, and D. W. Prather, “Radiofrequency signal-generation system with over seven octaves of continuous tuning,” *Nat. Photonics*, vol. 7, no. 2, pp. 118–122, Feb. 2013.
- [11] “10 GHz Lithium Niobate Modulators.” [Online]. Available: https://www.thorlabs.com/newgrouppage9.cfm?objectgroup_id=3918. [Accessed: 15-Nov-2018].
- [12] “Optilab - Devices - Optical Modulator.” [Online]. Available: http://www.optilab.com/devices/category/Optical_Modulator/. [Accessed: 15-Nov-2018].
- [13] “Phase Modulators,” *EOSPACE, INC.* [Online]. Available: <https://www.eospace.com/phase-modulator/>. [Accessed: 15-Nov-2018].
- [14] D. S. Smith, H. D. Riccius, and R. P. Edwin, “Refractive indices of lithium niobate,” *Opt. Commun.*, vol. 17, no. 3, pp. 332–335, Jun. 1976.
- [15] R. G. Hunsperger, *Integrated Optics: Theory and Technology*. Springer Science & Business Media, 2002.
- [16] R. C. Alferness, R. V. Schmidt, and E. H. Turner, “Characteristics of Ti-diffused lithium niobate optical directional couplers,” *Appl. Opt.*, vol. 18, no. 23, p. 4012, Dec. 1979.
- [17] K. Noguchi, O. Mitomi, and H. Miyazawa, “Millimeter-Wave Ti:LiNbO₃ Optical Modulators,” *J. Light. Technol.*, vol. 16, no. 4, p. 615, Apr. 1998.

- [18] P. G. Suchoski, T. K. Findakly, and F. J. Leonberger, "Stable low-loss proton-exchanged LiNbO₃ waveguide devices with no electro-optic degradation," *Opt. Lett.*, vol. 13, no. 11, pp. 1050–1052, Nov. 1988.
- [19] J. L. Jackel, C. E. Rice, and J. J. Veselka, "Proton exchange for high-index waveguides in LiNbO₃," *Appl. Phys. Lett.*, vol. 41, no. 7, pp. 607–608, Oct. 1982.
- [20] F. Caccavale *et al.*, "Secondary-ion-mass spectrometry and near-field studies of Ti:LiNbO₃ optical waveguides," *J. Appl. Phys.*, vol. 78, no. 9, pp. 5345–5350, Nov. 1995.
- [21] R. C. Alferness, "Titanium-Diffused Lithium Niobate Waveguide Devices," in *Sixth IEEE International Symposium on Applications of Ferroelectrics*, 1986, pp. 1–3.
- [22] M. Fontaine, A. Dela[^]ge, and D. Landheer, "Modeling of titanium diffusion into LiNbO₃ using a depth-dependent diffusion coefficient," *J. Appl. Phys.*, vol. 60, no. 7, p. 2343, 1986.
- [23] "Lithium Niobate Wafers," *Gooch & Housego*. [Online]. Available: <https://goochandhousego.com/product-categories/lm-wafers/>. [Accessed: 09-Nov-2018].
- [24] "Van der Waals force - an overview | ScienceDirect Topics." [Online]. Available: <https://www.sciencedirect.com/topics/pharmacology-toxicology-and-pharmaceutical-science/van-der-waals-force>. [Accessed: 10-Nov-2018].
- [25] "Encyclopedia of Laser Physics and Technology - free spectral range, resonator, cavity, axial mode spacing." [Online]. Available: https://www.rp-photonics.com/free_spectral_range.html. [Accessed: 10-Nov-2018].
- [26] H. Robinson, C. W. Pitt, and R. A. Gibson, "Silicon lithium niobate electro-optic waveguide modulator structures in the parallel-plate configuration," *Appl. Opt.*, vol. 32, no. 21, pp. 3981–3988, Jul. 1993.
- [27] T. A. Rost, H. Lin, T. A. Rabson, R. C. Baumann, and D. L. Callahan, "Deposition and analysis of lithium niobate and other lithium niobium oxides by rf magnetron sputtering," *J. Appl. Phys.*, vol. 72, no. 9, pp. 4336–4343, Nov. 1992.
- [28] A. R. Poghosyan, R. Guo, A. L. Manukyan, and S. G. Grigoryan, "Stoichiometric lithium niobate thin films preparation by sol-gel method," in *Photonic Fiber and Crystal Devices: Advances in Materials and Innovations in Device Applications*, 2007, vol. 6698, p. 66981C.
- [29] A. V. Prasada Rao, D. S. Paik, and S. Komarneni, "Sol-gel Synthesis of Lithium Niobate Powder and Thin Films Using Lithium 2,4-Pentanedionate as Lithium Source," *J. Electroceramics*, vol. 2, no. 3, pp. 157–162, Nov. 1998.
- [30] T. Hibiya *et al.*, "Liquid phase epitaxial growth and characterization of LiNbO₃ single crystal films," *J. Cryst. Growth*, vol. 144, no. 3, pp. 213–217, Dec. 1994.
- [31] S. Fushimi and K. Sugii, "Growth of Lithium Niobate Single Crystal by the Closed-Tube Sulphur Vapour Transport Technique," *Jpn. J. Appl. Phys.*, vol. 13, no. 11, p. 1895, Nov. 1974.

- [32] R. Baets *et al.*, “Silicon photonics: Silicon nitride versus silicon-on-insulator,” in *2016 Optical Fiber Communications Conference and Exhibition (OFC)*, 2016, pp. 1–3.
- [33] N. Sharma, M. Hooda, and S. K. Sharma, “Synthesis and Characterization of LPCVD Polysilicon and Silicon Nitride Thin Films for MEMS Applications,” *Journal of Materials*, 2014. [Online]. Available: <https://www.hindawi.com/journals/jma/2014/954618/>. [Accessed: 23-Oct-2017].
- [34] “LPCVD Nitride deposition - Wafer Services from Rogue Valley Microdevices,” *Rogue Valley Microdevices - Microelectronics Manufacturing*. .
- [35] B. Reynes and J. C. Bruyère, “High-density silicon nitride thin film in PECVD,” *Sens. Actuators Phys.*, vol. 32, no. 1, pp. 303–306, Apr. 1992.
- [36] N. Ahmed, C. B. Singh, S. Bhattacharya, S. Dhara, and P. B. Bhargav, “Raman and FTIR Studies on PECVD Grown Ammonia-Free Amorphous Silicon Nitride Thin Films for Solar Cell Applications,” *Conference Papers in Science*, 2013. [Online]. Available: <https://www.hindawi.com/journals/cpis/2013/837676/>. [Accessed: 11-Nov-2018].
- [37] K. Aoki, J. Kondou, O. Mitomi, and M. Minakata, “Velocity-Matching Conditions for Ultrahigh-Speed Optical LiNbO₃ Modulators with Traveling-Wave Electrode,” *Jpn. J. Appl. Phys.*, vol. 45, no. 11R, p. 8696, Nov. 2006.
- [38] R. Spickermann, S. R. Sakamoto, and N. Dagli, “In traveling wave modulators which velocity to match?,” in , *IEEE Lasers and Electro-Optics Society Annual Meeting, 1996. LEOS 96*, 1996, vol. 2, pp. 97–98 vol.2.
- [39] X. Tu *et al.*, “50-Gb/s silicon optical modulator with traveling-wave electrodes,” *Opt. Express*, vol. 21, no. 10, p. 12776, May 2013.